



Inferring and evaluating satellite-based constraints on NO_x emissions estimates in air quality simulations

James D. East^{1,2}, Barron H. Henderson³, Sergey L. Napelenok³, Shannon N. Koplitz³, Golam Sarwar³, Robert Gilliam³, Allen Lenzen⁴, Daniel Q. Tong⁵, R. Bradley Pierce⁴, and Fernando Garcia-Menendez¹

¹Department of Civil, Construction, and Environmental Engineering, North Carolina State University, Raleigh, NC 27606, USA

²Oak Ridge Institute for Science and Education, Office of Research and Development, U.S. Environmental Protection Agency, Research Triangle Park, NC 27711, USA

³U.S. Environmental Protection Agency, Research Triangle Park, NC 27711, USA

⁴Space Science and Engineering Center, University of Wisconsin-Madison, Madison, WI 53706, USA

⁵Department of Atmospheric, Oceanic and Earth Sciences, George Mason University, Fairfax, VA 22030, USA

Correspondence: Fernando Garcia-Menendez (f_garcia@ncsu.edu)

Received: 24 June 2022 – Discussion started: 25 July 2022

Revised: 28 October 2022 – Accepted: 9 November 2022 – Published: 20 December 2022

Abstract. Satellite observations of tropospheric NO_2 columns can provide top-down observational constraints on emissions estimates of nitrogen oxides (NO_x). Mass-balance-based methods are often applied for this purpose but do not isolate near-surface emissions from those aloft, such as lightning emissions. Here, we introduce an inverse modeling framework that couples satellite chemical data assimilation to a chemical transport model. In the framework, satellite-constrained emissions totals are inferred using model simulations with and without data assimilation in the iterative finite-difference mass-balance method. The approach improves the finite-difference mass-balance inversion by isolating the near-surface emissions increment. We apply the framework to separately estimate lightning and anthropogenic NO_x emissions over the Northern Hemisphere for 2019. Using overlapping observations from the Ozone Monitoring Instrument (OMI) and the Tropospheric Monitoring Instrument (TROPOMI), we compare separate NO_x emissions inferences from these satellite instruments, as well as the impacts of emissions changes on modeled NO_2 and O_3 . OMI inferences of anthropogenic emissions consistently lead to larger emissions than TROPOMI inferences, attributed to a low bias in TROPOMI NO_2 retrievals. Updated lightning NO_x emissions from either satellite improve the chemical transport model's low tropospheric O_3 bias. The combined lightning and anthropogenic emissions updates improve the model's ability to reproduce measured ozone by adjusting natural, long-range, and local pollution contributions. Thus, the framework informs and supports the design of domestic and international control strategies.

1 Introduction

Tropospheric nitrogen oxides (NO_x), nitric oxide (NO) and nitrogen dioxide (NO_2), harm human health (Anenberg et al., 2018; Murray et al., 2020) and play a key role in the formation of important secondary atmospheric pollutants, such as O_3 (Jacob, 2000). NO_x is emitted to the troposphere primarily by anthropogenic combustion processes, but natural sources, including soil, lightning, and wildfires, also contribute to the atmospheric NO_x budget (Jacob, 1999). Ac-

curate NO_x emissions are a critical component of local- to global-scale atmospheric chemistry simulations. On hemispheric scales, realistically representing the formation and intercontinental transport of O_3 with models requires adequate global emissions inventories (Itahashi et al., 2020; Zhang et al., 2016, 2008; Verstraeten et al., 2015; Mathur et al., 2017). In regional air quality simulations, which commonly rely on hemispheric or global models for chemical boundary conditions, the relative contribution of long-range

pollutant transport to ground-level O₃ concentrations has grown in many areas as O₃ precursor emissions have decreased in the US and other high-income countries (HICs) (McDuffie et al., 2020; Jaffe et al., 2018; Simon et al., 2015). As a result, air quality management policies, often informed by regional modeling, are strengthened by accurate and up-to-date global NO_x emissions inventories. However, compilation of bottom-up regional and global emissions inventories, developed from source- and location-specific emissions factors and activity data, is time- and labor-intensive and can be hindered by limited data. As a result, bottom-up inventories lag behind emissions changes and are often incomplete. Uncertainties in bottom-up emissions estimates are particularly large for lower-middle-income countries (McDuffie et al., 2020; Elguindi et al., 2020) and remain significant for HICs (Day et al., 2019).

Satellite observations of NO₂ can bridge temporal gaps in emissions estimates (Tong et al., 2016, 2015) and constrain uncertainty in emissions inventories through inverse modeling (e.g., Lamsal et al., 2011; Goldberg et al., 2021; de Foy and Schauer, 2022). Several methods have been applied to develop top-down emissions estimates using satellite observations and atmospheric models, each carrying advantages and limitations (Elguindi et al., 2020). Adjoint-based methods can provide precise emissions updates but require significant computational resources (e.g., Qu et al., 2017, 2019; Muller and Stavrakou, 2005; Kurokawa et al., 2009; Cooper et al., 2017; Zhang et al., 2019; Y. Wang et al., 2020). Similarly, Kalman filtering and related approaches have been used but are computationally intensive (e.g., Napelenok et al., 2008; Ding et al., 2020, 2015; Mijling and van der A, 2012; Miyazaki and Eskes, 2013; Miyazaki et al., 2017, 2012a, b; Sekiya et al., 2021). Mass-balance inversion approaches, which scale model emissions by directly comparing model estimates and satellite observations, were introduced by Martin et al. (2003), updated by Lamsal et al. (2011), and have been widely used in research and forecasting (e.g., Boersma et al., 2015; Itahashi et al., 2019; Li et al., 2018; Visser et al., 2019; Zhu et al., 2021; Cooper et al., 2017). Although lower computational costs allow the finite-difference mass-balance (FDMB) approach (Lamsal et al., 2011) to readily update emissions, the method is subject to an emissions-smearing effect (e.g., Cooper et al., 2017), which can cause emissions updates to be spatially misallocated. Since FDMB uses satellite observations directly, near-surface NO₂ bias cannot be isolated from biases in the middle and upper troposphere, which obscures the surface emissions inference. Further, applications often rely on a single inversion from a single satellite, although available satellite products have been shown to have significant biases. For example, early versions of the Tropospheric Monitoring Instrument (TROPOMI) NO₂ product showed a low bias in urban areas when compared against ground-based and airborne spectrometer measurements (Judd et al., 2020; Verhoelst et al., 2021), and the Ozone Monitoring Instrument

(OMI) NO₂ product has been reported to differ with measurements by $\pm 20\%$ (Lamsal et al., 2014). The impact of biases in satellite-based NO₂ data on mass-balance inversions has not been fully explored despite the wide use of the method to scale NO_x emissions. Minimizing biases in anthropogenic emissions inferences and understanding the potential for them to propagate to emissions updates are needed to improve mass-balance-based inversions.

Here, we introduce a modeling framework that couples satellite chemical data assimilation to the Community Multiscale Air Quality model (CMAQ) and applies an iterative FDMB inversion to estimate NO_x emissions in the Northern Hemisphere. The framework provides observational constraints to improve emissions estimates in areas where emissions are highly uncertain, at a lower computational cost relative to adjoint- and Kalman-filter-based approaches. We apply the framework in an iterative assimilation to infer 2019 NO_x emissions, the first complete year in which OMI and TROPOMI records overlap. In contrast to traditional FDMB approaches, which directly compares modeled and observed columns, our framework improves the FDMB method by first assimilating satellite-retrieved NO₂ and then performing the inversion by comparing model simulations with and without assimilation. In the assimilation step, updates to model concentrations are vertically allocated to model layers. As a result, assimilating the observed column allows the inversion framework to use only the near-surface portion of the model column in the FDMB inversion, minimizing influences from the upper troposphere and extending the framework proposed by Lamsal et al. (2011). In addition, our analysis compares independent inversions which separately use OMI or TROPOMI NO₂ data. We show that the inverse emissions produced by this framework influence the representation of intercontinental O₃ transport to the US, offering an opportunity to improve chemical boundary conditions in policy-relevant regional-scale air quality simulations.

2 Methods

We develop a framework to update NO_x emissions estimates using the CMAQ chemical transport air quality model (Byun and Schere, 2006), 3D variational (3DVAR) chemical data assimilation (Sandu and Chai, 2011), and space-based NO₂ observations. We apply the framework to estimate 2019 lightning and anthropogenic NO_x emissions and compare ground- and space-based NO₂ observations to model simulations using the prior emissions (inventory before the framework is applied) and posterior emissions (inventory after the framework is applied) to assess the impact of the updates. Figure 1 provides an overview of the framework, in which lightning NO_x (LNO_x) emissions and anthropogenic NO_x (ANO_x) emissions are updated separately.

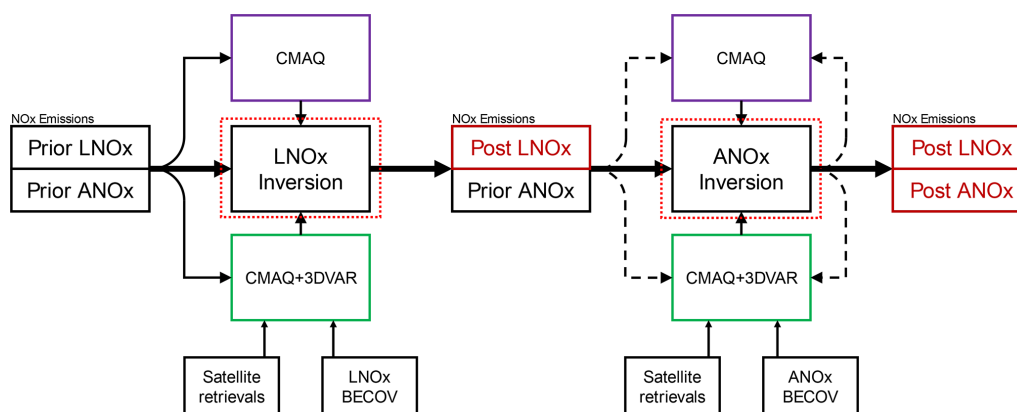


Figure 1. NO_x emissions inversion framework. Lightning NO_x (LNO_x) emissions are updated in the first step. Then, anthropogenic NO_x (ANO_x) emissions are updated iteratively. CMAQ boxes represent air quality simulations without chemical data assimilation, and CMAQ+3DVAR boxes represent air quality model simulations with chemical data assimilation. Satellite NO₂ retrievals and a background error covariance (BECOV) are inputs to the chemical data assimilation, described in Sect. 2.3. Red dotted lines around the inversion boxes correspond to the red dotted lines in Fig. 3, which details the inversion algorithm. Dashed black emissions input lines around the ANO_x inversion represent the iterative process. Iteration and convergence criteria are described in Sect. 2.6.

2.1 Satellite data

We use NO₂ tropospheric column observations from the National Aeronautics and Space Administration's (NASA's) OMI and from the Royal Netherlands Meteorological Institute's (KNMI's) TROPOMI instruments in the inversion framework. TROPOMI was launched in October 2017 and provides $7.2 \times 3.6 \text{ km}^2$ resolution NO₂ retrievals, upgraded to $5.6 \times 3.6 \text{ km}^2$ resolution in August 2019 (Van Geffen et al., 2020; Veefkind et al., 2012). TROPOMI's sun-synchronous polar orbit crosses the Equator at approximately 13:30 local time (LT), allowing the instrument to achieve global coverage in one day. We assimilate the Level-2 tropospheric slant column retrieved from NASA's Earth Science Data Systems program (<https://www.earthdata.nasa.gov/>, last access: 9 December 2022). The data product is described in the Algorithm and Theoretical Basis Document (ATBD) for TROPOMI NO₂ (Van Geffen et al., 2019). We only consider TROPOMI observations with a quality flag greater than 0.5 and a cloud fraction lower than 30 % in the assimilation, following data product recommendations (Eskes et al., 2019). We use the latest publicly available versions of the TROPOMI retrieval for 2019 (versions 1.2.2 to 1.3.2) at the time of the analysis. Version 1.3 introduced updates to cloud processing that decreased noisy hotspots and broadened the range of acceptable air mass factors (Eskes et al., 2021). Information about the updates applied in each version and the dates on which updates were applied is given in Eskes et al. (2021). A research version with an updated retrieval applied to 2019 observations has been developed (Van Geffen et al., 2022) but was not yet standard and was not available at the time of this analysis. We discuss the impact of these latest updates in Sect. 3.3.

OMI, on board the Aura satellite launched in 2004, provides tropospheric NO₂ vertical and slant column retrievals with a resolution of $13 \times 24 \text{ km}^2$ near nadir in a sun-synchronous polar orbit, with a local Equator crossing time of 13:45 LT. Global coverage is achieved in 2 d. We use the NASA Goddard Space Flight Center (GSFC) Level-2 NO₂ product (Krotkov et al., 2019b). OMI was impacted by a row anomaly beginning in 2008, reducing the number of usable pixels in the OMI retrieval (Boersma et al., 2018). We include only pixels with a cloud fraction lower than 30 % and a summary quality flag of 0. Detailed information about the NO₂ data product is included in the OMI ATBD (Chance, 2002) and in Krotkov et al. (2019a).

A low bias has been noted in the versions of TROPOMI NO₂ used for this study (Judd et al., 2020; Verhoelst et al., 2021). Although TROPOMI NO₂ retrievals from 2019 have been reprocessed with retrieval version 2.3.1, resulting in an improvement of the bias (Eskes et al., 2021), these reprocessed datasets were not yet available at the time this analysis was conducted. Figure 2 compares TROPOMI and OMI tropospheric vertical column densities (VCDs) for 2019, re-gridded to the CMAQ grid used. For the VCDs shown in the figure, we remove the effect of the assumed vertical profile of NO₂ from the original satellite product by recalculating the VCDs with the NO₂ vertical profile simulated by CMAQ. In the results, we discuss the low bias in TROPOMI data and explore its impact on emissions inversions.

2.2 Hemispheric air quality modeling

Model simulations in the inversion framework were completed for January–December 2019 using CMAQ v5.3.2 (Appel et al., 2021; U.S. EPA Office of Research and Development, 2020). CMAQ has been used to simulate air qual-

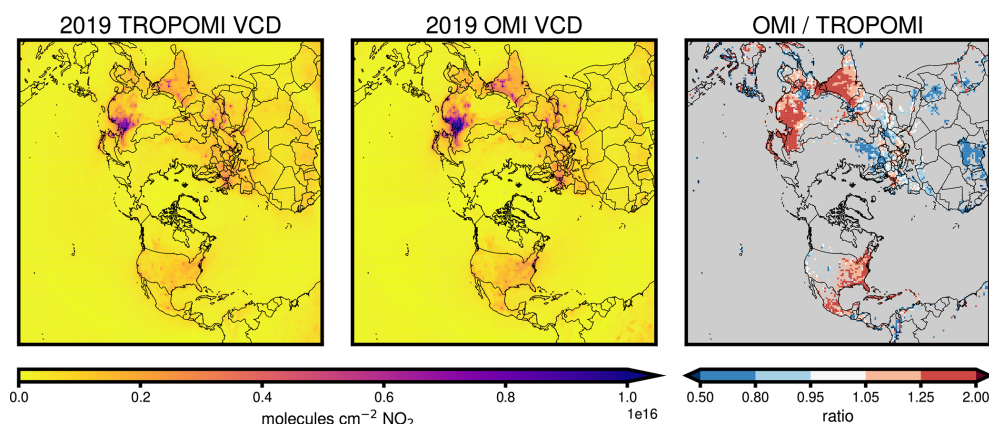


Figure 2. 2019 annual average TROPOMI and OMI vertical NO₂ vertical column densities, with CMAQ NO₂ profiles applied, and the ratio between them. Column density ratios are only shown for the grid cells where NO_x emissions updates are applied in the emissions inversion.

ity over the Northern Hemisphere and has been shown to adequately capture chemical composition against observations (Mathur et al., 2017). Model inputs and satellite observations are summarized in Table 1. Simulations, designed to capture continental-scale pollutant transport, cover the Northern Hemisphere with 108 km horizontal grid spacing and a 44-layer vertical structure reaching 50 hPa (Mathur et al., 2017). The simulations use version CB6r3 of the Carbon Bond 6 chemical mechanism (Luecken et al., 2019), the AERO7 aerosol module (Xu et al., 2018) and updated halogen chemistry (Kang et al., 2021). Anthropogenic emissions are modeled using representative day-of-week emissions that change month to month. Representative-day emissions are created by averaging data from the prior emissions inventory on a day-of-week basis by month. For each day of the week and each month, there is a unique hourly emissions file that is used for every matching day of the week in that month. As a result, diurnal and weekly patterns are captured in the emissions, while daily variations that are specific to the prior emissions inventory year are averaged. The prior emissions inventory relies on the best available emissions data at the time of the study. Anthropogenic emissions for North America are from the U.S. Environmental Protection Agency's (EPA) 2017 National Emissions Inventory (NEI) modeling platform (Adams, 2020). Emissions in China are for the year 2015 (Zhao et al., 2018), and emissions for the rest of the hemisphere are based on the Hemispheric Transport of Air Pollution (HTAP) version 2, projected from their original 2010 date to 2014, with scaling factors from the Community Emissions Data System (CEDS). To initialize the 2019 prior and posterior simulations and to reduce the impact of chemical initial conditions on the results, we use a 1-year spin-up period not considered for the analyses. CMAQ model runs are driven by meteorology from a retrospective hemispheric simulation using the Weather Research and Forecasting (WRF) model (Skamarock et al., 2008) ver-

sion 4.1.1, configured following Mathur et al. (2017) and Xing et al. (2015).

2.3 Chemical data assimilation in CMAQ

We adjust modeled NO₂ concentrations using satellite observations by coupling the CMAQ model to a data assimilation model, the National Centers for Environmental Prediction (NCEP) Gridpoint Statistical Interpolation (GSI) program version 3.3 (Shao et al., 2016). GSI performs 3D variational (3DVAR) data assimilation by minimizing the cost function, J :

$$J = \frac{1}{2} \left[\mathbf{x}^T \mathbf{B}^{-1} \mathbf{x} + (\mathbf{H}(\mathbf{x}) - \mathbf{y})^T \mathbf{R}^{-1} (\mathbf{H}(\mathbf{x}) - \mathbf{y}) \right], \quad (1)$$

where \mathbf{y} is the observation innovation $\mathbf{y} = \mathbf{y}_o - \mathbf{H}(\mathbf{x}_b)$, \mathbf{x} is the analysis increment $\mathbf{x} = \mathbf{x}_a - \mathbf{x}_b$, \mathbf{x}_a is the analysis field (NO₂ concentration after application of chemical data assimilation), \mathbf{x}_b is the model background (the simulated NO₂ concentration before application of chemical data assimilation), \mathbf{y}_o is the satellite observations, \mathbf{B} is the background error covariance matrix, \mathbf{R} is the observation error matrix, and \mathbf{H} is the observation operator. To compute the difference between the model column (\mathbf{x}_b) and the satellite column (\mathbf{y}_o), the observation operator \mathbf{H} is applied, which transforms the model background to the form of the satellite observations. For TROPOMI data, the averaging kernel is first converted to scattering weights as

$$\mathbf{w}(z) = \mathbf{A}(z) \times M_{\text{total}}, \quad (2)$$

where $\mathbf{A}(z)$ is the vertically resolved TROPOMI averaging kernel for level z , M_{total} is the air mass factor provided with the satellite data, and $\mathbf{w}(z)$ is the vertically resolved scattering weights. Scattering weights accompany the OMI NO₂ data product, so this step is not needed to assimilate OMI data. Scattering weights are then applied to compute the

Table 1. Prior emissions and model inputs.

Data	Year	Source
Prior emissions (North America)	2017 EPA platform (v7.1)	Adams (2020)
Prior emissions (China)	2015 Tsinghua University	Zhao et al. (2018)
Prior emissions (rest of hemisphere)	HTAPv2 (2010) projected to 2014 using CEDS scaling factors	Janssens-Maenhout et al. (2015), Hoesly et al. (2018)
Prior emissions (LNO _x)	2017 GEIA*	Price et al. (1997)
Biomass-burning emissions	2019 FINN*	Wiedinmyer et al. (2011)
Soil NO _x emissions	2018 CAMS* v2.1 with canopy reduction factor	Granier et al. (2019)
Biogenic emissions	2018 MEGAN*	Guenther et al. (2006)
Meteorology	2019 WRF v4.1.1	Powers et al. (2017)
Satellite observation year	2019 NO ₂ retrievals from OMI and TROPOMI	

* GEIA – Global Emissions Initiative; FINN – Fire Inventory from NCAR; CAMS – Community Atmosphere Modeling System; MEGAN – Model of Emissions of Gases and Aerosols from Nature

model slant column as

$$\Omega_s^m = \sum_z \Omega_v^m(z) \mathbf{w}(z), \quad z \leq z_{\text{tropopause}}, \quad (3)$$

where $\Omega_v^m(z)$ is the model partial vertical column in the troposphere, interpolated to the satellite grid, and Ω_s^m is the model tropospheric slant column density (SCD). The difference between the modeled and observed slant columns, or the observation innovation \mathbf{y} in Eq. (1), is estimated as

$$\Omega'_s = \Omega_v^o M_{\text{trop}} - \Omega_s^m, \quad (4)$$

where Ω'_s is the analysis increment, Ω_v^o is the satellite tropospheric VCD, and M_{trop} is the tropospheric air mass factor, distributed with the satellite data. We eliminate the influence of the a priori satellite vertical profile by computing the analysis increment with the modeled and observed SCD, which, unlike the VCD, does not rely on the a priori vertical NO₂ profile assumed by the satellite.

We compute \mathbf{B} using the Generalized Background Error covariance matrix model (GENBE v2.0) (Descombes et al., 2015), which models background errors by comparing a free-running simulation and a simulation with either lightning or anthropogenic NO_x emissions perturbed. We use GENBE with the prior simulation and a simulation with a uniform −15 % perturbation to LNO_x to create three-dimensional background errors in the upper troposphere for the LNO_x assimilation. After updating LNO_x emissions (as described in Sect. 2.5), we create three-dimensional background errors in the boundary layer for the anthropogenic NO_x assimilation by using GENBE with the LNO_x posterior simulation and a simulation with a −15 % perturbation to surface anthropogenic NO_x emissions. Observation error \mathbf{R} is provided with the satellite data.

Online coupling between GSI and CMAQ was developed in this study to perform the assimilation. At each model time step in which a satellite observation is available, the CMAQ model simulation is paused, and 3DVAR assimilation is performed. The CMAQ model state at that time step is used as \mathbf{x}_b . After assimilation using 3DVAR within GSI, CMAQ returns to a free-running mode, and the new model state, \mathbf{x} , is updated to more closely match the satellite observation. The difference in the monthly average NO₂ VCDs from the assimilation and no-assimilation runs is used in the inversion as $\Delta\Omega$.

2.4 Finite-difference mass-balance inversion

In the inversion framework developed, we iterate the approach of Lamsal et al. (2011). The FDMB process as applied here is summarized in Fig. 3. In the past, this approach has been used by directly comparing model and satellite columns (e.g., Itahashi et al., 2019; Cooper et al., 2017; Lamsal et al., 2011). We modify the approach by first updating model concentrations with assimilation of satellite observations and then updating the emissions using the difference between the modeled VCD with and without assimilated satellite information. All updates are performed on a monthly average basis.

In FDMB, following Lamsal et al. (2011), emissions changes are inferred through the relationship

$$\frac{\Delta E}{E} = \beta \frac{\Delta\Omega}{\Omega}, \quad (5)$$

where ΔE is the inferred NO_x emissions change, E is the NO_x emissions prior, Ω is the model simulated NO₂ VCD without chemical data assimilation, and $\Delta\Omega = \Omega_{\text{assim}} - \Omega$

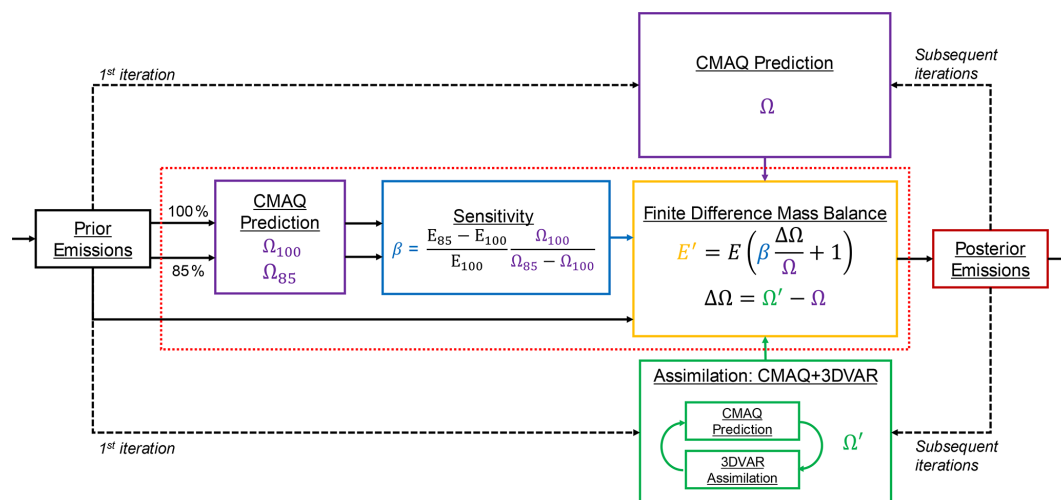


Figure 3. FDMB inversion. The red dashed line corresponds to the red dashed lines in Fig. 1, and the processes inside show additional details of the FDMB inversion. In this framework, the prior emissions (black box on the far left) are input to the CMAQ model. CMAQ simulations are performed with unperturbed prior emissions (100 % arrow and E_{100}) and prior emissions with a -15% perturbation (85 % arrow and E_{85}). The resulting modeled VCDs are Ω_{100} and Ω_{85} , respectively. These VCDs are used to compute the sensitivity, β (blue box). New emissions totals are calculated with FDMB (yellow box), using β , NO₂ VCD from a CMAQ simulation without assimilation (Ω), and NO₂ VCD from a CMAQ simulation with assimilation (Ω'). When iteration is used, the posterior emissions from the previous iteration are used as input to the CMAQ model to simulate new VCDs, Ω and Ω' .

is the monthly average difference between the model simulated tropospheric NO₂ VCD with (Ω_{assim}) and without (Ω) chemical data assimilation. β is a unitless scaling parameter, the Jacobian, that linearly relates NO₂ VCD changes to NO_x emissions changes. β is calculated through finite differencing as

$$\beta = \frac{E' - E}{E} \frac{\Omega_E}{\Omega_{E'} - \Omega_E}, \quad (6)$$

where E' is perturbed NO_x emissions, Ω_E is the tropospheric NO₂ VCD simulated with model emissions E , and $\Omega_{E'}$ is the tropospheric NO₂ VCD simulated with model emissions E' . To estimate β , we use the same -15% perturbation used to create background errors **B** in the boundary layer. Cooper et al. (2017) found that using perturbations ranging from 5 % to 20 % to calculate β changed posterior emissions estimates by less than 2 % globally.

2.5 Inverse modeling NO_x emissions

In our framework, LNO_x emissions are updated first, separately from anthropogenic emissions. Due to the satellite instruments' sensitivity to NO₂ in the upper atmosphere (e.g., Eskes and Boersma, 2003), small model biases there can influence the total column comparison and adversely impact the anthropogenic emissions adjustment. By updating LNO_x emissions, we aim to decrease this bias and its impact on the ANO_x inversion. We compute the scaling parameter for lightning emissions, β_{LNO_x} , using the -15% LNO_x perturbation simulations applied to create background errors for

the upper troposphere. We then assimilate satellite NO₂ observations using the background errors for the upper troposphere and apply β_{LNO_x} in a single inversion iteration using the full tropospheric VCD to compute spatially varying LNO_x adjustment factors. Updates to LNO_x are calculated using monthly averages.

After LNO_x emissions are updated, ANO_x emissions are updated by iteratively applying an FDMB inversion independently for each month in 2019. Iterating the FDMB has been shown to improve emissions estimates compared to a single FDMB application (Cooper et al., 2017). In the FDMB iteration, each update to the emissions serves as the prior emissions for the subsequent iteration (represented as black dashed lines in Fig. 1). The number of iterations is determined based on the synthetic observation experiment described in Sect. 2.6. β is held constant during all ANO_x inversion iterations and is not recalculated each time to prevent instability in β as changes in the column become smaller with subsequent iterations. In the ANO_x emissions inversion, we only consider grid cells in which local anthropogenic NO_x emissions likely contribute significantly to the satellite-observed NO₂ column by only including grid cells in which anthropogenic NO_x emissions comprise at least 50 % of total NO_x emissions, following Lamsal et al. (2011); population density is greater than 15 000 people km⁻² (CIESIN, 2018); modeled cloud cover is less than 30 %; and the local time is 13:00 or 14:00 (OMI and TROPOMI overpass times). Only emissions in grid cells meeting these criteria are adjusted. Table S1 in the Supplement describes each simulation performed for the LNO_x and ANO_x inversions.

The FDMB method assumes that emissions impacts are local (i.e., emissions in one grid cell do not affect VCD amounts in neighboring grid cells). This assumption is most valid when NO_x lifetime is shorter than NO_x transport time to neighboring grid cells, which is typical near the surface in coarse-resolution models (Martin et al., 2003), such as the one used in this study. However, the assumption is less realistic at finer resolutions and in the upper troposphere, where the lifetime of NO₂ is longer than at the surface and where NO₂ concentrations are not directly impacted by coincident near-surface emissions. Even at coarse resolutions (e.g., 100 km grid spacing), emissions-smearing effects, which occur when the FDMB assumption of local emissions effects is incorrect and emissions are inappropriately adjusted, can appear due to NO_x transport, reservoir species, and chemical feedbacks (Turner et al., 2012; Cooper et al., 2017). Traditional FDMB, which directly compares modeled and remotely sensed columns, cannot address this effect. Assimilating the satellite VCD introduces an additional complication. The horizontal length scales (on the order of several hundreds of kilometers) used in the background error extend beyond the grid cell horizontal dimensions (nominally 108 km) in the middle and upper troposphere; as a result, NO₂ changes introduced by assimilation ($\Delta\Omega$) do not have a local relationship with surface emissions directly below. In our work, assimilating the observed column information instead of directly comparing modeled and satellite-retrieved VCDs allows the analysis to be restricted to the lower troposphere, mitigating both the misallocation errors of FDMB and the effect of horizontal length scales extending beyond the grid cell dimension. To that end, we limit the anthropogenic emissions analysis to the lowest 20 model layers, which is nominal from the ground to ~ 720 hPa over non-mountainous terrain in the summer, and use that partial column to calculate $\Delta\Omega$ in the FDMB inversion. $\Delta\Omega$ for a single month above and below the threshold is illustrated in Fig. S1 in the Supplement. By applying this cutoff, we focus the inversion on surface anthropogenic NO_x.

2.6 Inversion system testing

We conduct a synthetic observation experiment to evaluate the ability of the inversion system to constrain emissions to a known perturbation. Artificial NO₂ observations were generated from CMAQ simulations with unperturbed emissions and NO_x emissions reduced by 15 %. As expected, assimilating the synthetic observations derived from a simulation with unperturbed emissions results in an analysis increment of zero. The results of an iterative emissions inversion based on the synthetic observations derived from the simulation with perturbed emissions are shown in Fig. S2. Across Northern Hemisphere regions, the normalized mean error (NME) relative to the known perturbed emissions and the rate at which it changes decrease with subsequent iterations. The NME is minimized after seven to nine iterations, depending on the

region. In all subsequent results, emissions inferences made with eight iterations of the inversion system are shown and analyzed. Convergence of the inversion in different global regions adds confidence to the system's ability to constrain real-world emissions.

3 Results

3.1 Lightning NO_x emissions updates

Assimilation of retrievals from either satellite increases LNO_x emissions across all seasons, relative to the prior emissions (monthly climatology from GEIA), with the largest changes occurring during the summer (Figs. S3 and S4). Applying 2019 OMI data increases total LNO_x emissions in 2019 by 20 % over the GEIA climatology, while assimilation of TROPOMI data increases LNO_x emissions by 24 %. The emissions increases inferred by both satellite products are driven by NO₂ increases in the mid and upper troposphere due to assimilation, with changes near the surface being negligible in comparison. Increases in background areas with small NO₂ column totals and subsequent LNO_x increases in these areas suggest a low bias in modeled background NO₂ relative to observations from both satellites. A low bias agrees with the findings reported by other model and satellite NO₂ comparisons (Silvern et al., 2019; Qu et al., 2021; Goldberg et al., 2017). The LNO_x emissions adjustments inferred here decrease the differences between modeled and satellite-derived NO₂ in the upper troposphere and decrease the bias that differences in the upper troposphere can introduce to the subsequent ANO_x inversion.

3.2 Impact of assimilation on modeled NO₂ vertical column density

Figure 4 shows the change to CMAQ-modeled tropospheric VCD, ($\Delta\Omega$) caused by assimilating NO₂ observations from OMI or TROPOMI with background errors for the boundary layer, before applying any emissions adjustments. In Fig. 4 and throughout the results, $\Delta\Omega$ reflects differences near the surface (as described in Sect. 2.5). Assimilating OMI NO₂ data generally increases modeled NO₂ columns near populated areas in China, India, and the US. In contrast, assimilating TROPOMI NO₂ data decreases modeled NO₂ columns more widely across the Northern Hemisphere. The changes brought about by assimilating satellite data are larger during the winter and fall and smaller in the spring and summer, when NO_x lifetime is shortest and when NO₂ columns are smaller. During the winter in northeast China, where the assimilation impacts are most apparent, the seasonal average change due to assimilation reaches 1.8×10^{15} molec. cm⁻² for OMI and -2.8×10^{15} molec. cm⁻² for TROPOMI. The direction of $\Delta\Omega$ after assimilation of OMI data is more heterogeneous and shows a stronger seasonality, while $\Delta\Omega$ based on assimilating TROPOMI data is consistently nega-

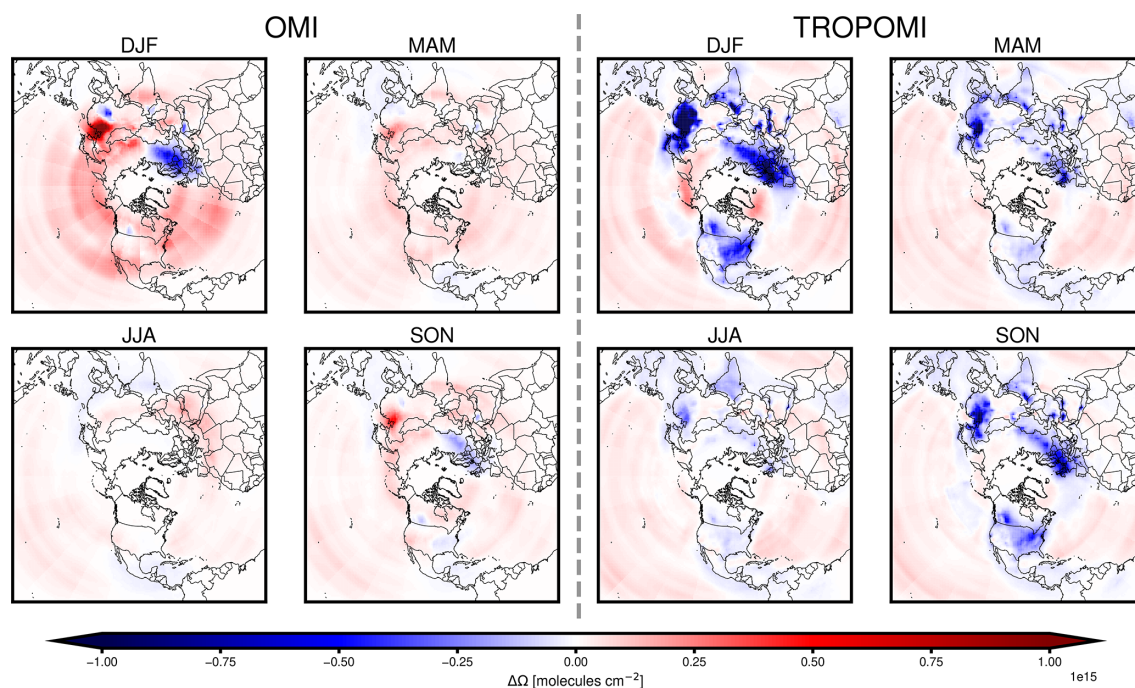


Figure 4. Seasonal NO₂ VCD change ($\Delta\Omega$) from CMAQ simulation using prior emissions after assimilating OMI or TROPOMI tropospheric NO₂ observations and modeling atmospheric composition with prior NO_x emissions. $\Delta\Omega$ shown for winter (DJF), spring (MAM), summer (JJA), and fall (SON).

tive. Over Europe, $\Delta\Omega$ after assimilating OMI observations is close to zero in warm months and negative in colder seasons. Assimilating satellite-observed NO₂ increases the NO₂ levels modeled over the ocean and less-populous areas, such as the Sahara, with low NO_x emissions and small NO₂ column amounts.

Over polluted areas, the direction of $\Delta\Omega$ for the TROPOMI or OMI data assimilations tends to differ. This discrepancy is likely due to the low bias in TROPOMI-derived tropospheric NO₂ columns, which has been reported to be approximately 10 % over the US, Europe, and India, and greater than 20 % over China when compared with the OMI Quality Assurance for Essential Climate Variables (QA4ECV) retrieval (Van Geffen et al., 2022; Verhoelst et al., 2021; C. J. Wang et al., 2020; Li et al., 2021). Over background areas, the analysis increments that result from assimilation of observations from both satellites generally agree. The consistency suggests a low bias in modeled background NO₂ concentrations and also agrees with the low bias in CMAQ-modeled free-tropospheric NO₂ reported by Goldberg et al. (2017). Such a bias can contribute to the positive analysis increment over background areas. However, NO₂ columns observed in these regions may be smaller than the retrieval accuracy of 0.7×10^{15} molec. cm⁻² (Van Geffen et al., 2019), reducing confidence in the analysis increment at these locations. In the anthropogenic emissions inversion, our filtering criteria exclude background areas which are more likely to have low VCD amounts.

3.3 Emissions inversion

Season-average β values, relating NO₂ vertical column differences to anthropogenic near-surface NO_x emissions updates, are shown in Fig. S5. Based on our criteria for grid cell inclusion in the inversion, described in Sect. 2.5, we consider 13 % of the grid cells in the domain, which represent 88 % of prior anthropogenic NO_x emissions. Seasonal domain-average values range from 1.33 to 1.66 and are lower in the winter and higher in the summer. A β value less than 1.0 results in an emissions update that is smaller than the VCD change, while a β greater than 1.0 has the opposite effect. β tends to be less than 1.0 in polluted regions during colder months and larger during warmer months and in less-polluted regions, although many grid cells which are less polluted are not considered in the analysis. The scaling factors are smallest over China and larger over the US, India, Mexico, and Europe. The differences among regions stem from local differences in NO_x lifetime and transport. In Indonesia and sub-Saharan Africa, lower emissions and a small response from tropospheric VCD to anthropogenic emissions perturbations can lead to large β values. To prevent overly large or small β values, we constrain the factor to between 0.1 and 10, following Cooper et al. (2017). Scaling factors estimated here are larger than the 1.16 global-average previously reported by Lamsal et al. (2011). However, in Lamsal et al. (2011), modeled NO₂ vertical columns were sampled at the morning SCanning Imaging Absorption spectroMeter

for Atmospheric CHartographY (SCIAMACHY) overpass time rather than at the afternoon OMI or TROPOMI overpass times; β tended to be closer to 1.0 during the morning in regions with high NO_x emissions (Li and Wang, 2019). Li and Wang (2019) show that, over rural regions with lower NO_x concentrations, β is larger at the OMI or TROPOMI overpass window than at the SCIAMACHY overpass window, suggesting that a larger overall β for analyses based on OMI or TROPOMI products should be expected. Additionally, NO_x emissions have decreased considerably in several regions of the Northern Hemisphere, including the US (Tong et al., 2015) and China (Miyazaki et al., 2017), after the Lam-sal (2011) study was conducted, which has changed the sensitivity of NO₂ VCDs to NO_x emissions (Qu et al., 2021; Silvern et al., 2019).

Annual bottom-up prior ANO_x emissions estimates are shown in Fig. 5. Season-average ANO_x emissions inferences from the inversions based on OMI and TROPOMI observations are shown in Fig. 6. The use of OMI observations generally tends to increase emissions in most industrialized nations outside of Europe. NO_x emissions increases driven by OMI observations are largest in winter and spring and smaller, or slightly decreased, in summer and fall. In contrast, the use of TROPOMI retrievals tends to drive a decrease in NO_x emissions across all seasons and continents, with the largest impacts in the summer and the smallest in the spring. The largest emissions changes based on both OMI and TROPOMI retrievals are in northeast China during the winter. Over India, OMI-inferred changes are concentrated in central India, where prior emissions are lower, while the largest changes inferred from TROPOMI are in the northern, eastern, and southern zones, where prior emissions are highest. Relative NO_x emissions changes driven by TROPOMI observations tend to be small over dense urban areas, with more uniform decreases over cells with lower emissions.

ANO_x emissions totals and inferred changes are explored for China, India, Europe, Mexico, and the US (Fig. 7). We also show 2019 NO_x emissions totals from the Copernicus Atmosphere Monitoring Service's (CAMS's) bottom-up emissions inventory (Granier et al., 2019) and from the NASA Tropospheric Chemical Reanalysis products 2 (TCR-2) satellite-inferred inventory (Miyazaki et al., 2019, 2020). TCR-2 top-down NO_x emissions are constrained using satellite observations of NO₂, CO, O₃, and SO₂ at a resolution of $1.125^\circ \times 1.125^\circ$ and are further described in Miyazaki et al. (2017). CAMS anthropogenic NO_x emissions are based on the Emissions Database for Global Atmospheric Research (EDGAR version 5.3) estimates for 2015 (Crippa et al., 2020), projected to 2019 using CEDS scaling factors, and are provided at $0.1^\circ \times 0.1^\circ$. Both datasets provide monthly anthropogenic NO_x totals. Except for Europe, assimilation toward OMI retrievals increases annual emissions totals in the regions analyzed, while using TROPOMI retrievals decreases them. TCR-2 NO_x emissions estimates are larger than the prior emissions used by our inverse modeling frame-

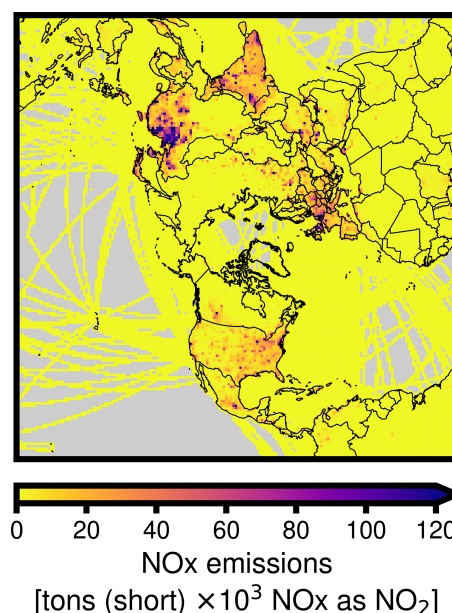


Figure 5. 2019 prior anthropogenic NO_x emissions totals. Data sources are described in Table 1.

work, except for India, while CAMS totals are lower than the prior emissions estimates and are similar to TROPOMI inferred emissions. Across the regions considered, TROPOMI infers an average annual decrease of -33% in NO_x emissions from the regions, while OMI infers a $+9\%$ increase. In Europe, the only region where the sign of the inferred changes match, the use of OMI retrievals results in a -1% change, while applying TROPOMI observations leads to a -36% decrease in NO_x emissions. The largest total changes are inferred in the highest-emitting region, China, while the greatest relative changes, -41% inferred with TROPOMI, are for India, where emissions are highly uncertain. Changes inferred with OMI observations over the US are greater than 1200×10^3 short tons NO_x as NO₂ per year but smaller than the difference between our prior US emissions estimates and TCR-2 or CAMS estimates. A change of -3000×10^3 short tons NO_x as NO₂ emitted annually in the US, as inferred by TROPOMI, over 30 % of the prior emissions differs significantly from National Emissions Inventory estimates but leads to a total close to that of the 2019 CAMS inventory.

Across the months simulated, inferences using OMI retrievals consistently lead to higher NO_x emissions than using TROPOMI retrievals. Figure 8 shows monthly NO_x emissions totals and inferred changes for several global regions. The magnitude of changes is generally smallest in summer months and largest in winter months for both OMI- and TROPOMI-inferred emissions. Monthly prior emissions totals lay between the OMI and TROPOMI inferences, except for summertime emissions in India and Mexico, where both satellite inferences decrease NO_x emissions. Over Europe, both satellite products infer a decrease during the winter, al-

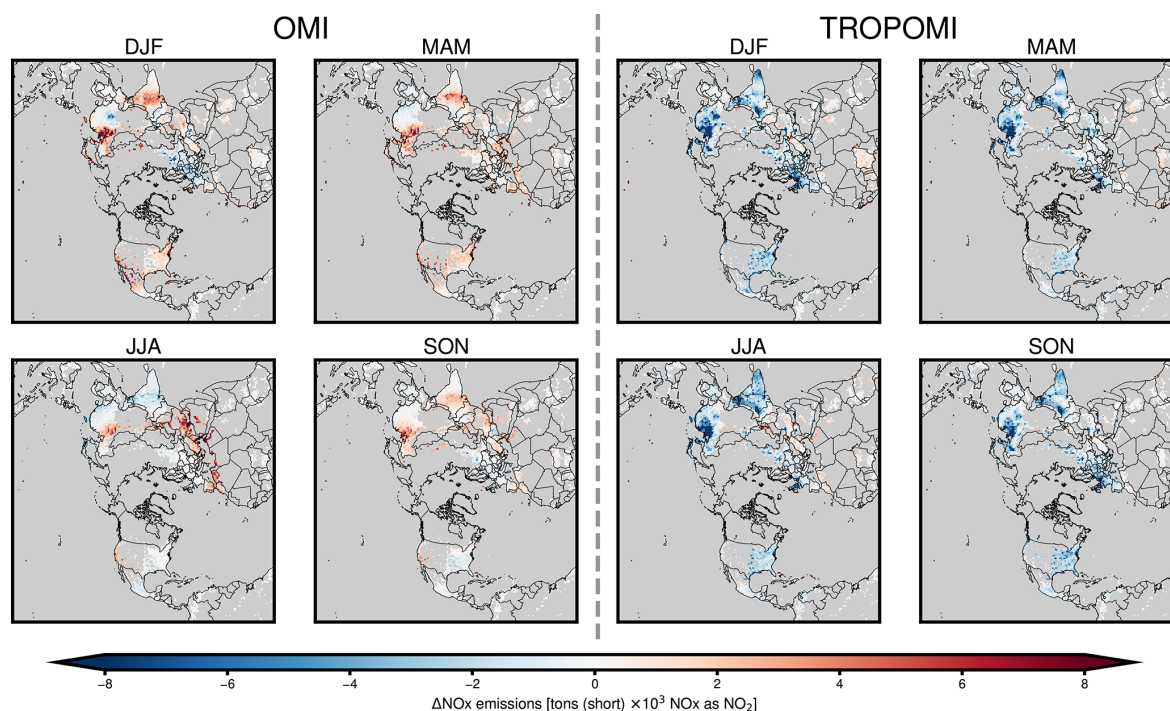


Figure 6. Season-average NO_x emissions changes from inverse modeling updates based on OMI and TROPOMI observations. Emissions changes are shown for winter (DJF), spring (MAM), summer (JJA), and fall (SON).

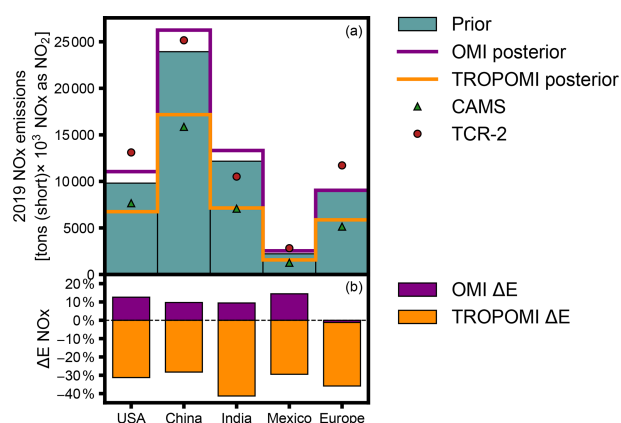


Figure 7. Prior and satellite-inferred 2019 anthropogenic NO_x emissions in select global regions. Plot (a) shows total emissions (as NO₂) from prior emissions estimates, inference with OMI or TROPOMI observations (OMI and TROPOMI posterior), and CAMS or TCR-2 inventories in the US, China, India, Mexico, and Europe. Plot (b) shows the percent change (ΔENO_x) inferred with OMI or TROPOMI data, relative to prior emissions estimates, for each region.

though fewer valid satellite pixels due to snow cover at high latitudes and longer winter NO₂ atmospheric lifetimes may influence the inference.

Based on reported NO_x emissions trends (McDuffie et al., 2020; U.S. EPA, 2022a), changes from the prior emis-

sions inventory (Table 1) to 2019 are expected. Relative to the prior emissions, significant decreases in NO_x emissions in China, estimated for 2015 in the prior inventory, and smaller reductions in Europe and North America, reported for 2014 and 2017 in the prior inventory, respectively, should be anticipated. TROPOMI-inferred emissions reflect the direction anticipated for these changes but with larger than expected magnitudes. For example, the 28 % decrease in anthropogenic NO_x emissions over China between 2015 and 2019 inferred from the TROPOMI observations is substantially larger than the 8 % decrease estimated between 2015 and 2017 by the Community Emissions Data System (McDuffie et al., 2020). Bottom-up estimates indicate that anthropogenic NO_x emissions in the US have decreased through 2019 (U.S. EPA, 2022a). Although the direction of the emissions change inferred from TROPOMI agrees with the trend in bottom-up estimates, its magnitude is larger than expected. An underestimation of US emissions in winter in the prior inventory when compared with OMI inferences contrasts with field study results reporting no bias in north-eastern US winter emissions estimates (Jaegle et al., 2018; Salmon et al., 2018). In India, bottom-up emissions inventories report sustained growth of NO_x emissions (Kurokawa and Ohara, 2020; McDuffie et al., 2020), and NO₂ levels observed by OMI have been increasing since 2005 (Goldberg et al., 2021; Cooper et al., 2022). The decrease in anthropogenic NO_x emissions inferred by TROPOMI observations

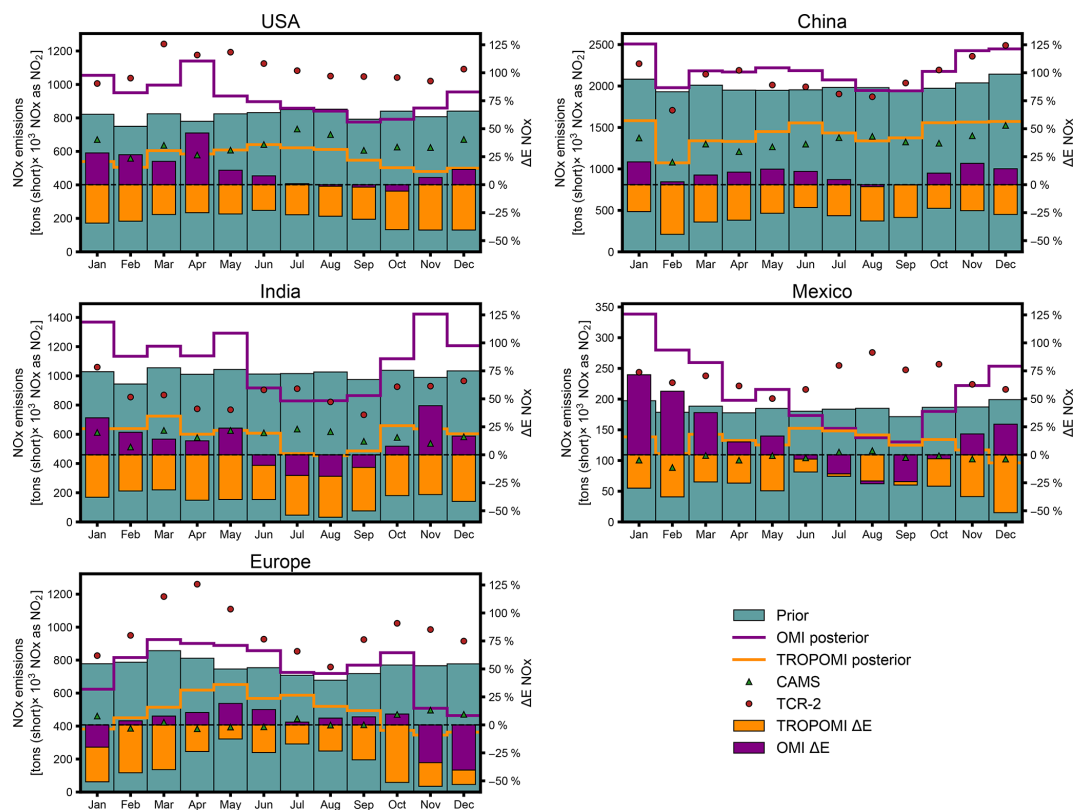


Figure 8. Monthly prior and satellite-inferred anthropogenic NO_x emissions in 2019 in select global regions. Total monthly emissions (as NO_2) from prior emissions estimates, inference with OMI or TROPOMI observations (OMI and TROPOMI posterior), and CAMS or TCR-2 inventories in the US, China, India, Mexico, and Europe are shown. Percent changes (ΔENox) inferred with OMI or TROPOMI data, relative to prior emissions estimates, for each region are shown by the purple and orange bars.

contrasts with these trends in bottom-up estimates and OMI observations.

The low bias known to affect TROPOMI NO_2 observations influences the results of the emissions inversion, which targets grid cells with high emissions, likely leading to decreases in inferred emissions that are larger than expected. We conduct an inversion using the reprocessed TROPOMI NO_2 version 2.3.1 (Van Geffen et al., 2022) to infer NO_x emissions for January 2019 and find that the updated data increase the TROPOMI posterior inference by 17 % over the US and 4 % in China relative to version 1.2.2. While using the updated retrievals shrinks the gap between OMI- and TROPOMI-inferred emissions, it does not change the overall trend of smaller posterior emissions using TROPOMI NO_2 (Figs. S10 and S11). The differences between emissions inferred by OMI and TROPOMI observations highlight the importance of ongoing efforts to harmonize OMI and TROPOMI NO_2 retrieval algorithms, such as the NASA Multi-Decadal Nitrogen Dioxide and Derived Products from Satellites (MINDS) (Lamsal et al., 2020) and the QA4ECV (Boersma et al., 2017) datasets.

In addition to smearing effects, coarse-resolution models can artificially alter nonlinear NO_2 chemistry, leading to

biases in inferences of NO_x emissions from satellite NO_2 columns (Valin et al., 2011; Sekiya et al., 2021; Lamsal et al., 2011). Higher-resolution simulations can better resolve β and reduce biases caused by nonlinear chemistry. Additional errors in the emissions estimates may be associated with emissions from non-anthropogenic NO_x sources. Although the emissions inversion targets anthropogenic sources only, changes in NO_2 columns observed by the satellite instruments driven by natural NO_x emissions processes may not be captured in the air quality model simulations and subsequently lead to biased anthropogenic emissions inferences (Li et al., 2021).

The emissions resulting from the inverse modeling framework are comparable to CAMS and TCR-2 2019 emissions estimates in several ways. In the US, China, and Europe, the magnitudes of ANO_x emissions from OMI retrievals are comparable to TCR-2 NO_x emissions estimates and exhibit similar monthly patterns. Annual NO_x emissions inferred from OMI observations are also relatively similar to TCR-2 estimates for India and Mexico, although monthly emissions patterns differ. Unlike TCR-2 emissions estimates, which are also constrained by OMI NO_2 observations, 2019 CAMS emissions estimates are projected from 2015 bottom-up data.

However, CAMS estimates provide a representation of anticipated emissions trends. In all regions considered, CAMS NO_x emissions estimates are close to the TROPOMI inference annual totals and lower than the prior emissions, OMI inferences, and TCR-2 estimates, potentially suggesting that global NO_x emissions have not decreased as much as anticipated by the CAMS inventory projections.

3.4 Impacts of emissions updates on modeled NO₂ and O₃

We evaluate and compare the CMAQ simulations' ability to reproduce observed pollutant concentrations when driven with NO_x emissions estimates from the prior inventory and with those derived by the inverse modeling framework. Figure 9 compares 2019 OMI and TROPOMI NO₂ VCD retrievals with modeled NO₂ VCDs using the prior emissions with no updates, LNO_x emissions updates, and LNO_x and ANO_x emissions updates. Satellite-based LNO_x emissions updates improve CMAQ model performance – correlation coefficient (*R*), normalized mean error (NME), and normalized mean bias (NMB) – when evaluated against tropospheric VCD retrievals, relative to model performance with the prior emissions. OMI-inferred ANO_x emissions updates further improve CMAQ model performance evaluated against VCD retrievals, decreasing NMB from −20 % to −5 % and NME from 38 % to 28 %. Model performance is improved by using OMI data in the inverse modeling framework across all seasons (Figs. S6–S9). Although LNO_x emissions updates derived from TROPOMI observations improve model bias and error relative to the CMAQ simulation using prior emissions estimates, TROPOMI-inferred anthropogenic emissions do not, except during summer months (Figs. 9 and S6–S9). The lack of significant improvements in CMAQ-simulated NO₂ VCDs after applying the emissions inversion with TROPOMI NO₂ retrievals prior to the version 2.3.1 update (Van Geffen et al., 2022) may be associated with changing chemical regimes that are not captured in the emissions inversion process.

Changes in modeled VCD due to assimilation and the emissions inferences calculated in the TROPOMI ANO_x inversion exceed the emissions perturbation and VCD changes used to calculate β . For example, over the eastern US, the −15 % emissions perturbation used to calculate β leads to VCD changes of −15 % on average in winter, but assimilating TROPOMI retrievals leads to VCD changes ($\Delta\Omega$) of −19 % on average in the winter, with individual changes exceeding −30 %. Modeled NO_x chemistry and NO₂ vertical profiles after assimilating TROPOMI retrievals may be different than those used in the calculation of β . As a result, assimilating TROPOMI retrievals in the ANO_x inversion may lead to modeled NO₂ vertical profiles which are inconsistent with the precalculated β used in the FDMB relationship and to less reliable subsequent emissions inferences. In contrast, the magnitude of VCD changes due to assimilating OMI re-

trievals over the eastern US in winter is 8 %, well within the magnitude of the VCD changes used to precalculate β . This highlights the importance of applying a β sensitivity valid for the magnitude of anticipated emissions changes in FDMB inversions and the potential consequences of relying on satellite-derived retrievals with pre-existing biases in emissions inversions.

Comparing CMAQ-modeled O₃ to ozonesonde measurements from the World Ozone and Ultraviolet Radiation Data Centre (WOUDC) network shows the impacts updating LNO_x emissions on simulated tropospheric O₃ (Fig. 10). Above 300 hPa, the model is biased low, but neither update has a major impact on this bias. However, within the free troposphere, the effects of LNO_x emissions updates are larger. LNO_x satellite-inferred emissions from both satellites increase O₃ and subsequently improve the model's low O₃ bias across all seasons, with the strongest effect in the summer. This suggests a low background NO₂ in our prior simulation, consistent with several studies demonstrating that models underestimate background NO₂ (Goldberg et al., 2017; Qu et al., 2021; Silvern et al., 2019).

Comparisons of CMAQ-modeled NO₂ and O₃ concentrations with ground-level measurements highlight the challenges of reproducing local air quality with a coarse scale model but suggest potential to improve model performance with satellite-derived NO_x emissions updates. Table 2 shows statistics evaluating modeled ground-level daily average NO₂ and maximum 8 h O₃ concentrations over the US against observations from 1218 monitoring sites in the Air Quality System (AQS) (U.S. EPA, 2022b), excluding near-road monitors for which the gridded NO₂ fields are not representative. Statistics for each season are included in Tables S2 and S3. There is a significant low bias in CMAQ-predicted ground-level NO₂ concentrations compared with monitoring site measurements, likely due to the model's coarse grid resolution and the aggregation of NO₂ monitors within urban areas with high NO_x emissions and large concentration gradients. CMAQ simulations at higher horizontal resolution do not show the same bias against NO₂ surface observations (Toro et al., 2021). Agreement between modeled and observed ground-level NO₂ concentrations is improved by using OMI-inferred NO_x emissions compared with the prior emissions simulation, particularly during winter and spring months. Model performance evaluated against ground-level O₃ measurements improves to a smaller extent with OMI-inferred NO_x emissions during winter and spring months. The use of TROPOMI-inferred emissions has mixed impacts on CMAQ performance against observed ground-level NO₂ and O₃ concentrations, leading to limited gains in seasonal *R* and some seasonal biases and errors but also less agreement with observations for other seasonal statistics. In the US, the network of ground-based air quality observations is relatively large. However, in some regions where emissions uncertainties are expected to be especially high, ground-based observations are significantly limited and less accessible. Assess-

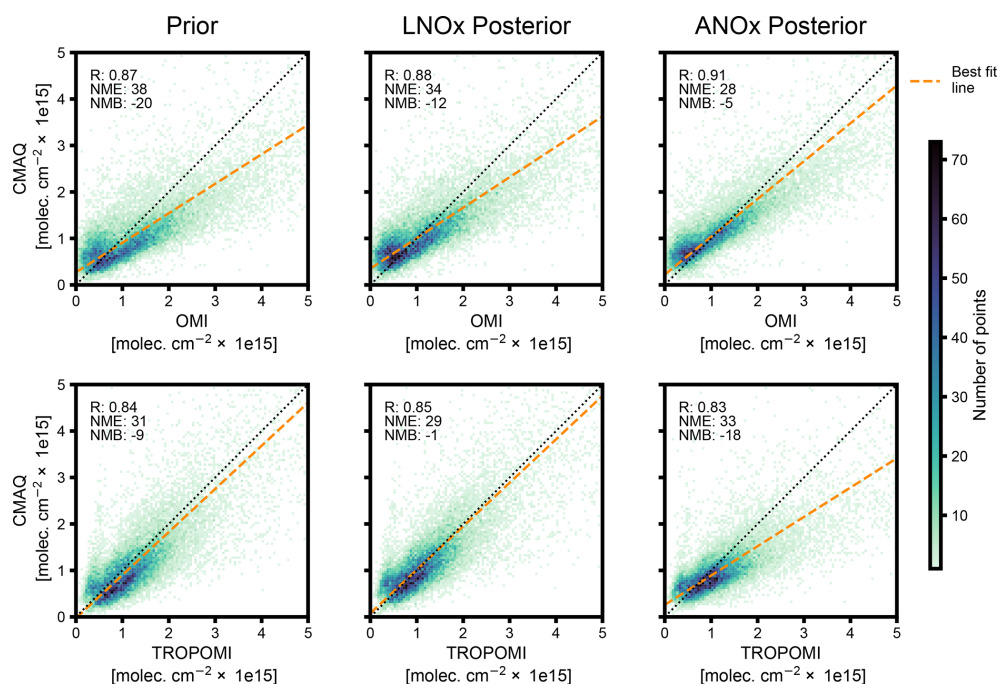


Figure 9. Impact of NO_x emissions updates on modeled NO_2 VCDs. Plots compare 2019 season-average CMAQ-modeled NO_2 VCD at each model grid cell in which NO_x emissions were updated by the inverse modeling framework against OMI and TROPOMI tropospheric NO_2 VCD retrievals averaged in each model grid cell. Modeled NO_2 VCD using prior emissions (Prior), inferred LNO $_x$ emissions (LNO $_x$ posterior), and inferred lightning and anthropogenic NO_x emissions (ANO $_x$ posterior) are each compared with NO_2 VCD retrievals. Top-row plots compare retrievals and modeled VCD based on OMI observations, while bottom-row plots compare retrievals and modeled VCD based on TROPOMI observations. Linear regression line, correlation coefficient (R), normalized mean error (NME), and normalized mean bias (NMB), relative to tropospheric NO_2 VCD retrievals, are shown for each CMAQ simulation.

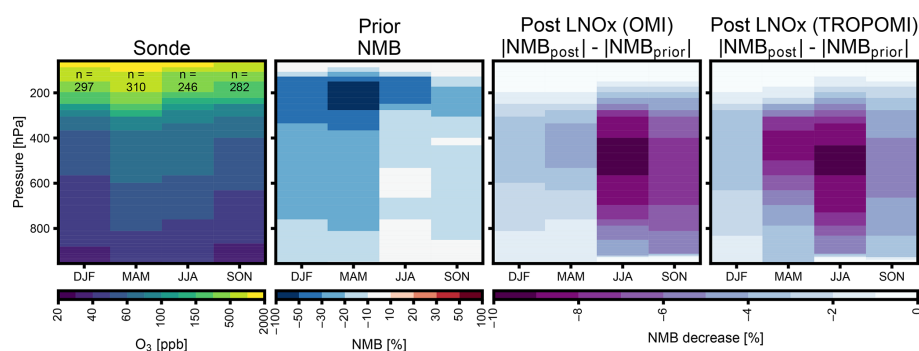


Figure 10. Ozonesonde observations from the WUOUC network and impact of lightning emissions inferences on modeled ozone. Left plot shows sonde observations averaged in each season and total number of launches per season. The NMB is shown for the prior emissions simulation. Plots on the right show the decrease in the NMB, relative to the prior simulation for simulations, with LNO $_x$ emissions updated with OMI and TROPOMI data.

ing the impact of emissions updated against ground-based observations in these regions, although a challenge, would provide further evaluation of the inversion framework in locations where satellite retrievals have the largest potential to provide important constraints to emissions estimates.

3.5 Impacts of emissions updates on long-range O_3 transport

Global NO_x emissions estimates affect model simulations of long-range air pollution transport. To explore these impacts, we examine the response of CMAQ-modeled trans-Pacific O_3 to the inverse modeling framework's NO_x emissions updates. Figure 11 shows season-average changes in simulated free-tropospheric O_3 over the North Pacific Ocean resulting

Table 2. CMAQ model performance evaluated against daily average NO₂ (DA NO₂) and maximum 8 h O₃ concentrations (MDA8 O₃) observed in 2019 by AQS monitoring sites in the US. Near-road monitors are not considered. Statistics are shown for simulations using prior emissions (Prior), lightning and anthropogenic NO_x emissions inferred with OMI data (OMI-inferred), and lightning and anthropogenic NO_x emissions inferred with TROPOMI data (TROPOMI-inferred). Coefficient of determination (*R*), normalized mean error (NME), and normalized mean bias (NMB), relative to AQS observations, are estimated for each CMAQ simulation.

Pollutant	NO _x emissions	<i>R</i>	NME	NMB
MDA8 O ₃	Prior	0.65	15.9 %	−1.4 %
	OMI-inferred	0.68	15.4 %	3.4 %
	TROPOMI-inferred	0.68	15.3 %	−3.3 %
DA NO ₂	Prior	0.45	62.2 %	−56.9 %
	OMI-inferred	0.52	57.4 %	−49.6 %
	TROPOMI-inferred	0.45	71.7 %	−69.9 %

from the use of OMI- and TROPOMI-inferred ANO_x emissions relative to the emissions simulation with LNO_x emissions updated. As expected, the emissions inversions lead to O₃ variations that follow NO_x emissions changes inferred for each satellite's observations, with OMI inferences resulting in higher O₃ concentrations and TROPOMI inferences resulting in lower O₃ concentrations over the North Pacific Ocean. Season-average differences with respect to the prior emissions simulation are as large as +1.8 ppb in winter, using OMI-based updates, and −1.9 ppb in spring, using TROPOMI-based updates. Combined with trans-Pacific wind patterns, the effects of the NO_x emissions inversions on modeled O₃ suggest potential implications of uncertain Asian emissions estimates for US air quality management and emphasize the impacts of biases in satellite retrievals on inverse modeling systems.

At the Trinidad Head, California, a location where atmospheric composition is relatively unaffected by local emissions sources and is responsive to trans-Pacific pollution transport (Fig. 11), differences in modeled daily average free-tropospheric O₃ concentrations can reach +5 or −3 ppb. Figure 12 compares CMAQ-modeled vertical O₃ profiles to observations from 39 ozonesondes launched at Trinidad Head in 2019 (WOUDC, 2019). Relative to the CMAQ simulation using prior emissions, NO_x emissions updates inferred from OMI and TROPOMI data can improve the model's ability to reproduce ozonesonde O₃ distributions measured from the site, in particular during winter and spring, when the discrepancies between modeled and observed concentrations are largest. These impacts on modeled vertical O₃ profiles are largely driven by changes the modeling framework's updates to lightning NO_x emissions. The inferred LNO_x increases from each satellite improve O₃ biases, while subsequent anthropogenic updates have smaller impacts, suggesting that biases in O₃ could be driven by background NO₂ composition in the model and not solely by long-range transport resulting from anthropogenic emissions.

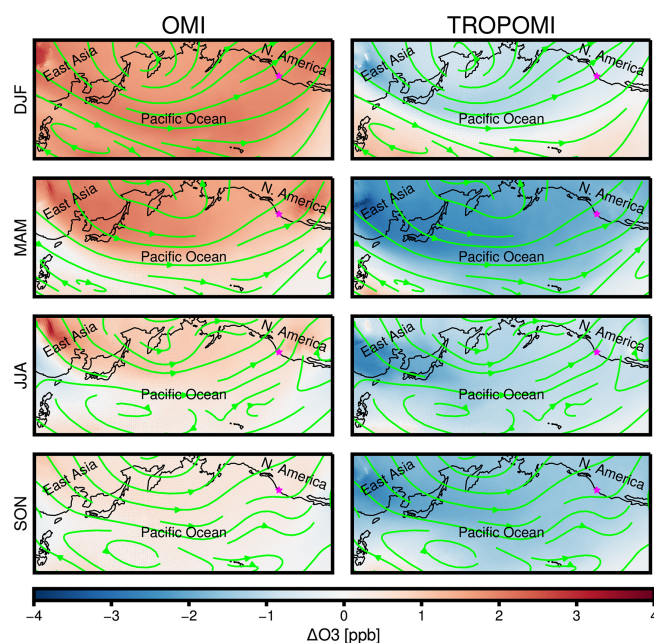


Figure 11. Changes in 2019 season-average free-tropospheric O₃ concentrations (averaged between 750 and 250 hPa) simulated over the North Pacific Ocean using lightning and anthropogenic NO_x emissions inferred with OMI or TROPOMI observations, relative to simulations using prior ANO_x emissions and updated LNO_x emissions. Differences are shown for winter (DJF), spring (MAM), summer (JJA), and fall (SON). Arrows depict season-average free-tropospheric winds (750–250 hPa). Star marker indicates location of Trinidad Head, California.

4 Conclusions

In this study, we describe a satellite chemical data assimilation and inverse emissions modeling framework based on the CMAQ hemispheric air quality modeling platform. In the framework, data assimilation adjusts modeled NO₂ concentrations online using satellite retrievals of tropospheric NO₂ VCDs. The NO₂ column changes drive the FDMB inversion, resulting in satellite-constrained top-down emissions esti-

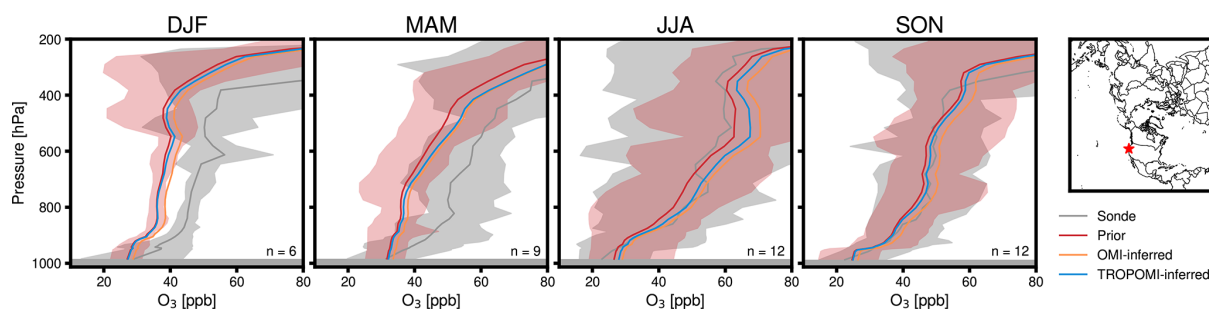


Figure 12. Season-average vertical O₃ concentration profiles modeled by CMAQ and measured by ozonesondes launched at Trinidad Head, California, in 2019. Vertical distributions are shown for simulations using prior emissions (Prior), lightning and anthropogenic NO_x emissions inferred with OMI data (OMI-inferred), and lightning and anthropogenic NO_x emissions inferred with TROPOMI data (TROPOMI-inferred). Modeled season-average profiles are shown during winter (DJF), spring (MAM), summer (JJA), and fall (SON) for days and times matching ozonesonde launches. Shading around sonde and prior emissions profiles represent the maximum and minimum O₃ at each pressure level. Map shows location of the Trinidad Head launch site.

mates. Here, we implement the framework in a NO_x emissions inversion to separately update 2019 Northern Hemisphere lightning and anthropogenic NO_x emissions estimates using NO₂ products from the OMI and TROPOMI satellite instruments. Relative to the modeling platform's prior emissions derived from regional and global emissions inventories, updates inferred using OMI and TROPOMI observations change average anthropogenic NO_x emissions by -41% to $+12\%$ in China, the US, India, Europe, and Mexico. Evaluated against ground-based NO₂ observations recorded over the US in 2019, the model performs best when using OMI-updated emissions, although a low bias in CMAQ predictions using prior emissions persists into simulations with satellite data assimilation. Compared with US ground-based O₃ observations, satellite-inferred emissions have mixed impacts on model performance, improving agreement with the measurements during certain months. LNO_x emissions inferences improve modeled O₃ when compared against ozonesonde observations across the Northern Hemisphere. The framework's NO_x emissions updates also affect model estimates of trans-Pacific O₃ transport, a source of growing concern in the US, with changes ranging from -3 to $+5$ ppb in simulated O₃ at a remote West Coast site, resulting from the use of satellite-inferred emissions.

The modeling framework presented has several limitations. The computational cost is greater than that of traditional FDMB inversions due to the assimilation step. However, the computational burden is comparable or less than other satellite assimilation methods such as Kalman-filter and adjoint 4D variational approaches. In addition, the framework requires minimal code changes to the underlying CTM, so inverse estimates will improve as the underlying air quality model is updated, with little additional effort needed to implement this framework. The global coverage of instruments on polar-orbiting satellites, such as Aura and Sentinel-5P, makes the emissions inversions possible but does not allow satellite observations to inform diurnal emissions vari-

ations. Upcoming geostationary satellite missions, including GEMS, TEMPO, and Sentinel-4, will provide this capability. Our approach, which balances computational costs and precision in the inversion, is subject to several assumptions. As in all mass-balance-based approaches, our method fully attributes the change in the VCD to emissions changes. To the extent that column differences are due to chemistry or transport and not emissions, this assumption introduces error into mass-balance inversions, including the inversion implemented in our framework. Large changes to the model concentrations resulting from the chemical data assimilation may invalidate assumptions in the subsequent FDMB inversion, leading to biases in the inferred emissions. The FDMB inversion treats each grid cell independently and cannot relate NO₂ column changes in one grid cell to emissions in another. Although emissions smearing in the approach is mitigated by only analyzing the lower portion of the model column, our emissions changes may be less precise than targeted assimilation methods, such as 4DVAR adjoint-based methods. Further, coarse grid resolution exacerbates biases in modeled NO₂ columns (Valin et al., 2011) and inferred NO_x emissions (Sekiya et al., 2021). The air quality model used here does not include stratospheric chemistry, which could affect comparisons against NO₂ retrievals. Nevertheless, the framework shows the potential to improve air quality model predictions using satellite-derived emissions updates, in particular for regions with uncertain emissions inventories or undergoing rapid emissions changes (Elguindi et al., 2020).

Emissions inversions based on satellite observations can provide valuable information for air quality modeling by addressing the gaps in bottom-up emissions inventories. However, our analysis shows that such inversions and subsequent air quality simulations can be strongly influenced by uncertainties and biases in the satellite data products used. In the analysis conducted, NO_x emissions inferred from TROPOMI observations appear to be biased low when assessed against those inferred from OMI data and surface and concentra-

tion measurements. The bias is consistent with recent research showing a low bias in TROPOMI v1.2 and v1.3 tropospheric columns (Judd et al., 2020; Verhoelst et al., 2021; Li et al., 2021; Van Geffen et al., 2022). The results highlight the importance of efforts to develop robust and consistent satellite data products for use in air quality modeling evaluation, assimilation, and emissions inversions. Ongoing efforts to this end include the MINDS (Lamsal et al., 2020) and the QA4ECV (Boersma et al., 2017) projects. This study also emphasizes the need for longer-term satellite data assimilation and comparisons of established and new satellite data products. The framework introduced here can serve as a generalized tool, with applications beyond those explored in this study, and allows new satellite data products to be incorporated as they become available. As satellite data products evolve and advance, the emissions inferred by the framework will improve.

Code and data availability. NO_x emissions data derived from this research are available from the authors upon request. Level-2 satellite retrievals are available from NASA's Goddard Earth Sciences Data and Information Services Center for OMI (<https://doi.org/10.5067/Aura/OMI/DATA2017>; Krotkov et al., 2019b) and TROPOMI version 1 (https://disc.gsfc.nasa.gov/datasets/S5P_L2_NO2___1/summary; last access: 9 December 2022; <https://doi.org/10.5270/S5P-s4ljg54>; Copernicus, 2018). TROPOMI retrievals reprocessed to version 2.3.1 are available through the Sentinel-5P data portal (<https://data-portal.s5p-pal.com/browser/>, last access: 9 December 2022; <https://doi.org/10.5270/S5P-9bnp8q8>; Copernicus, 2021). Woudc ozonesonde data, including data at the Trinidad Head, California, launch site, are available through Woudc at <https://doi.org/10.14287/10000008> (Woudc, 2019). Hourly AQS O₃ and NO₂ observations are available from EPA's Air Data website (https://aq5.epa.gov/aq5web/airdata/download_files.html, last access: 9 December 2022; U.S. EPA, 2022b). GSI code is available via <https://dtcenter.org/community-code/gridpoint-statistical-interpolation-gsi/download> (last access: 9 December 2022; DTC, 2018). CMAQ source code is freely available via <https://github.com/usepa/cmaq.git> (last access: 9 December 2022) and via the U.S. EPA Office of Research and Development (2020; <https://doi.org/10.5281/zenodo.4081737>).

Supplement. The supplement related to this article is available online at: <https://doi.org/10.5194/acp-22-15981-2022-supplement>.

Author contributions. JDE, BHH, SLN, SNK, and FGM designed the study. RBP, BHH, and DQT provided the initial conceptualization for the research. JDE conducted the air quality simulations, data assimilation, emissions inversions, and data analysis. AL developed the OMI and TROPOMI observation operators in GSI. BHH and JDE developed the CMAQ and GSI coupling. RG performed the meteorological modeling. GS implemented the halogen chemistry in the CMAQ model. JDE, BHH, SLN, SNK, RBP, and

FGM participated in data analysis and discussions. JDE wrote the paper with input from all co-authors.

Competing interests. The contact author has declared that none of the authors has any competing interests.

Disclaimer. The views expressed in this article are those of the authors and do not necessarily represent the views or policies of the U.S. Environmental Protection Agency.

Publisher's note: Copernicus Publications remains neutral with regard to jurisdictional claims in published maps and institutional affiliations.

Acknowledgements. James D. East was supported, in part, by an appointment to the Research Participation Program at the Office of Research and Development, U.S. Environmental Protection Agency, administered by the Oak Ridge Institute for Science and Education through an interagency agreement between the U.S. Department of Energy and the EPA. Daniel Q. Tong and R. Bradley Pierce acknowledge financial support from the NASA Health and Air Quality Applied Sciences Team (HAQAST) Tiger Team (award no. 80NSSC21K0427). We gratefully acknowledge the free availability and use of observational data sets from AQS and Woudc; remote sensing retrievals from OMI and TROPOMI; and global emission inventories from CAMS, TCR-2, and GEIA. Comments by Heather Simon and Tanya Spero at the U.S. EPA served to strengthen this manuscript.

Financial support. This research has been supported by the National Aeronautics and Space Administration (award no. 80NSSC21K0427).

Review statement. This paper was edited by Qiang Zhang and reviewed by two anonymous referees.

References

- Adams, E.: 2017 v1 NEI Emissions Modeling Platform (Premerged CMAQ-ready Emissions), Vesion V1, UNC Dataverse [dataset], <https://doi.org/10.15139/S3/TCR6BB>, 2020.
- Anenberg, S. C., Henze, D. K., Tinney, V., Kinney, P. L., Raich, W., Fann, N., Malley, C. S., Roman, H., Lamsal, L., Duncan, B., Martin, R. V., van Donkelaar, A., Brauer, M., Doherty, R., Jonson, J. E., Davila, Y., Sudo, K., and Kuylenstierna, J. C. I.: Estimates of the Global Burden of Ambient PM_{2.5}, Ozone, and NO₂ on Asthma Incidence and Emergency Room Visits, *Environ. Health Persp.*, 126, 107004, <https://doi.org/10.1289/Ehp3766>, 2018.
- Appel, K. W., Bash, J. O., Fahey, K. M., Foley, K. M., Gilliam, R. C., Hogrefe, C., Hutzell, W. T., Kang, D., Mathur, R., Murphy, B. N., Napelenok, S. L., Nolte, C. G., Pleim, J. E., Pouliot, G. A., Pye, H. O. T., Ran, L., Roselle, S. J., Sarwar, G., Schwede, D. B., Sidi, F. I., Spero, T. L., and Wong, D. C.: The Community

- Multiscale Air Quality (CMAQ) model versions 5.3 and 5.3.1: system updates and evaluation, *Geosci. Model Dev.*, 14, 2867–2897, <https://doi.org/10.5194/gmd-14-2867-2021>, 2021.
- Boersma, K. F., Vinken, G. C. M., and Tournadre, J.: Ships going slow in reducing their NO_x emissions: changes in 2005–2012 ship exhaust inferred from satellite measurements over Europe, *Environ Res Lett*, 10, 074007, <https://doi.org/10.1088/1748-9326/10/7/074007>, 2015.
- Boersma, K. F., Eskes, H., Richter, A., De Smedt, I., Lorente, A., Beirle, S., Van Geffen, J., Peters, E., Van Roozendaal, M., and Wagner, T.: QA4ECV NO₂ tropospheric and stratospheric vertical column data from SCIAMACHY, Version 1.1, Royal Netherlands Meteorological Institute (KNMI) [data set], <https://doi.org/10.21944/qa4ecv-no2-omi-v1.1>, 2017.
- Boersma, K. F., Eskes, H. J., Richter, A., De Smedt, I., Lorente, A., Beirle, S., van Geffen, J. H. G. M., Zara, M., Peters, E., Van Roozendaal, M., Wagner, T., Maasakkers, J. D., van der A, R. J., Nightingale, J., De Rudder, A., Irie, H., Pinardi, G., Lambert, J.-C., and Compernelle, S. C.: Improving algorithms and uncertainty estimates for satellite NO₂ retrievals: results from the quality assurance for the essential climate variables (QA4ECV) project, *Atmos. Meas. Tech.*, 11, 6651–6678, <https://doi.org/10.5194/amt-11-6651-2018>, 2018.
- Byun, D. and Schere, K. L.: Review of the governing equations, computational algorithms, and other components of the models-3 Community Multiscale Air Quality (CMAQ) modeling system, *Appl. Mech. Rev.*, 59, 51–77, <https://doi.org/10.1115/1.2128636>, 2006.
- Chance, K. (Ed.): OMI Algorithm Theoretical Basis Document, OMI Trace Gas Algorithms, Version 2.0, Smithsonian Astrophysical Observatory, Cambridge, MA, USA, Report no. ATBD-OMI-04, 78 pp., https://docsserver.gesdisc.eosdis.nasa.gov/repository/Mission/OMI/3.3_ScienceDataProductDocumentation/3.3.4_ProductGenerationAlgorithm/ATBD-OMI-04.pdf (last access: 9 December 2022), 2002.
- CIESIN (Center for International Earth Science Information Network – Columbia University): Gridded Population of the World, Version 4 (GPWv4): Population Density, Revision 10, NASA Socioeconomic Data and Applications Center (SEDAC) [dataset], Palisades, NY, <https://doi.org/10.7927/H4NP22DQ>, 2018.
- Cooper, M., Martin, R. V., Padmanabhan, A., and Henze, D. K.: Comparing mass balance and adjoint methods for inverse modeling of nitrogen dioxide columns for global nitrogen oxide emissions, *J. Geophys. Res.-Atmos.*, 122, 4718–4734, <https://doi.org/10.1002/2016jd025985>, 2017.
- Cooper, M. J., Martin, R. V., Hammer, M. S., Levelt, P. F., Veefkind, P., Lamsal, L. N., Krotkov, N. A., Brook, J. R., and McLinden, C. A.: Global fine-scale changes in ambient NO₂ during COVID-19 lockdowns, *Nature*, 601, 380–387, <https://doi.org/10.1038/s41586-021-04229-0>, 2022.
- Copernicus: Sentinel-5P TROPOMI Tropospheric NO₂ 1-Orbit L2 7km x 3.5km, Goddard Earth Sciences Data and Information Services Center (GES DISC) [data set], Greenbelt, MD, USA, <https://doi.org/10.5270/S5P-s4ljg54> (data available at: https://disc.gsfc.nasa.gov/datasets/S5P_L2_NO2____1/summary, last access: 9 December 2022), 2018.
- Copernicus: Copernicus Sentinel-5P (processed by ESA), TROPOMI Level 2 Nitrogen Dioxide total column products, Version 02, European Space Agency [data set], <https://doi.org/10.5270/S5P-9bnp8q8> (data available at: <https://data-portal.s5p-pal.com/browser/>, last access: 9 December 2022), 2021.
- Crippa, M., Solazzo, E., Huang, G. L., Guizzardi, D., Koffi, E., Muntean, M., Schieberle, C., Friedrich, R., and Janssens-Maenhout, G.: High resolution temporal profiles in the Emissions Database for Global Atmospheric Research, *Sci. Data*, 7, 121, <https://doi.org/10.1038/s41597-020-0462-2>, 2020.
- Day, M., Pouliot, G., Hunt, S., Baker, K. R., Beardsley, M., Frost, G., Mobley, D., Simon, H., Henderson, B. B., Yelverton, T., and Rao, V.: Reflecting on progress since the 2005 NARSTO emissions inventory report, *J. Air Waste Manage.*, 69, 1023–1048, <https://doi.org/10.1080/10962247.2019.1629363>, 2019.
- de Foy, B. and Schauer, J. J.: An improved understanding of NO_x emissions in South Asian megacities using TROPOMI NO₂ retrievals, *Environ. Res. Lett.*, 17, 024006, <https://doi.org/10.1088/1748-9326/ac48b4>, 2022.
- Descombes, G., Auligné, T., Vandenberghe, F., Barker, D. M., and Barré, J.: Generalized background error covariance matrix model (GEN_BE v2.0), *Geosci. Model Dev.*, 8, 669–696, <https://doi.org/10.5194/gmd-8-669-2015>, 2015.
- DTC (Developmental Testbed Center): Gridpoint Statistical Interpolation (GSI), DTC [code], <https://dtcenter.org/community-code/gridpoint-statistical-interpolation-gsi/download> (last access: 9 December 2022), 2018.
- Ding, J., van der A, R. J., Mijling, B., Levelt, P. F., and Hao, N.: NO_x emission estimates during the 2014 Youth Olympic Games in Nanjing, *Atmos. Chem. Phys.*, 15, 9399–9412, <https://doi.org/10.5194/acp-15-9399-2015>, 2015.
- Ding, J., van der A, R. J., Eskes, H. J., Mijling, B., Stavrakou, T., van Geffen, J. H. G. M., and Veefkind, J. P.: NO_x Emissions Reduction and Rebound in China Due to the COVID-19 Crisis, *Geophys. Res. Lett.*, 47, e2020GL089912, <https://doi.org/10.1029/2020GL089912>, 2020.
- Elguindi, N., Granier, C., Stavrakou, T., Darras, S., Bauwens, M., Cao, H., Chen, C., van der Gon, H. A. C. D., Dubovik, O., Fu, T. M., Henze, D. K., Jiang, Z., Keita, S., Kuenen, J. J. P., Kurokawa, J., Liousse, C., Miyazaki, K., Muller, J. F., Qu, Z., Solmon, F., and Zheng, B.: Intercomparison of Magnitudes and Trends in Anthropogenic Surface Emissions From Bottom-Up Inventories, Top-Down Estimates, and Emission Scenarios, *Earth's Future*, 8, e2020EF001520, <https://doi.org/10.1029/2020EF001520>, 2020.
- Eskes, H. J. and Boersma, K. F.: Averaging kernels for DOAS total-column satellite retrievals, *Atmos. Chem. Phys.*, 3, 1285–1291, <https://doi.org/10.5194/acp-3-1285-2003>, 2003.
- Eskes, H. J., van Geffen, J., Boersma, K. F., Eichmann, K. U., Apituley, A., Pedernana, M., Sneep, M., Veefkind, J. P., and Diego, L.: S5P/TROPOMI Level-2 Product User Manual – Nitrogen Dioxide, Royal Netherlands Meteorological Institute, S5P-KNMI-L2-0021-MA, 168 pp., 2019.
- Eskes, H. J., Eichmann, K. U., Lambert, J. C., Loyola, D., Veefkind, J. P., Dehn, A., and Zehner, C.: S5P/TROPOMI NO₂ Level 2 Product Readme File, Sentinel-5P Mission Performance Centre, S5P-MPC-KNMI-PRF-NO₂, 23 pp., 2021.
- Goldberg, D. L., Lamsal, L. N., Loughner, C. P., Swartz, W. H., Lu, Z., and Streets, D. G.: A high-resolution and observationally constrained OMI NO₂ satellite retrieval, *Atmos. Chem.*

- Phys., 17, 11403–11421, <https://doi.org/10.5194/acp-17-11403-2017>, 2017.
- Goldberg, D. L., Anenberg, S. C., Lu, Z. F., Streets, D. G., Lamsal, L. N., McDuffie, E. E., and Smith, S. J.: Urban NO_x emissions around the world declined faster than anticipated between 2005 and 2019, *Environ. Res. Lett.*, 16, 115004, <https://doi.org/10.1088/1748-9326/ac2c34>, 2021.
- Granier, C., Darras, S., Denier van der Gon, H., Doubalova, J., Elguindi, N., Galle, B., Gauss, M., Guevara, M., Jalkanen, J.-P., Kuenen, J., Liousse, C., Quack, B., Simpson, D., and Sindelarova, K.: The CAMS global and regional emissions (April 2019 version), Copernicus Atmosphere Monitoring Service, <https://doi.org/10.24380/d0bn-kx16>, 2019.
- Guenther, A., Karl, T., Harley, P., Wiedinmyer, C., Palmer, P. I., and Geron, C.: Estimates of global terrestrial isoprene emissions using MEGAN (Model of Emissions of Gases and Aerosols from Nature), *Atmos. Chem. Phys.*, 6, 3181–3210, <https://doi.org/10.5194/acp-6-3181-2006>, 2006.
- Hoesly, R. M., Smith, S. J., Feng, L., Klimont, Z., Janssens-Maenhout, G., Pitkanen, T., Seibert, J. J., Vu, L., Andres, R. J., Bolt, R. M., Bond, T. C., Dawidowski, L., Kholod, N., Kurokawa, J.-I., Li, M., Liu, L., Lu, Z., Moura, M. C. P., O'Rourke, P. R., and Zhang, Q.: Historical (1750–2014) anthropogenic emissions of reactive gases and aerosols from the Community Emissions Data System (CEDS), *Geosci. Model Dev.*, 11, 369–408, <https://doi.org/10.5194/gmd-11-369-2018>, 2018.
- Itahashi, S., Yumimoto, K., Kurokawa, J. I., Morino, Y., Nagashima, T., Miyazaki, K., Maki, T., and Ohara, T.: Inverse estimation of NO_x emissions over China and India 2005–2016: contrasting recent trends and future perspectives, *Environ. Res. Lett.*, 14, 124020, <https://doi.org/10.1088/1748-9326/ab4d7f>, 2019.
- Itahashi, S., Mathur, R., Hogrefe, C., Napelenok, S. L., and Zhang, Y.: Modeling stratospheric intrusion and trans-Pacific transport on tropospheric ozone using hemispheric CMAQ during April 2010 – Part 2: Examination of emission impacts based on the higher-order decoupled direct method, *Atmos. Chem. Phys.*, 20, 3397–3413, <https://doi.org/10.5194/acp-20-3397-2020>, 2020.
- Jacob, D. J.: Global Budget of Nitrogen Oxides, in: *Introduction to Atmospheric Chemistry*, 1st edn., Princeton University Press, Princeton, NJ, 213 pp., ISBN: 978-0-691-00185-2, 1999.
- Jacob, D. J.: Heterogeneous chemistry and tropospheric ozone, *Atmos. Environ.*, 34, 2131–2159, [https://doi.org/10.1016/S1352-2310\(99\)00462-8](https://doi.org/10.1016/S1352-2310(99)00462-8), 2000.
- Jaegle, L., Shah, V., Thornton, J. A., Lopez-Hilfiker, F. D., Lee, B. H., McDuffie, E. E., Fibiger, D., Brown, S. S., Veres, P., Sparks, T. L., Ebben, C. J., Wooldridge, P. J., Kenagy, H. S., Cohen, R. C., Weinheimer, A. J., Campos, T. L., Montzka, D. D., Digangi, J. P., Wolfe, G. M., Hanisco, T., Schroder, J. C., Campuzano-Jost, P., Day, D. A., Jimenez, J. L., Sullivan, A. P., Guo, H., and Weber, R. J.: Nitrogen Oxides Emissions, Chemistry, Deposition, and Export Over the Northeast United States During the WINTER Aircraft Campaign, *J. Geophys. Res.-Atmos.*, 123, 12368–12393, <https://doi.org/10.1029/2018jd029133>, 2018.
- Jaffe, D. A., Cooper, O. R., Fiore, A. M., Henderson, B. H., Tonnesen, G. S., Russell, A. G., Henze, D. K., Langford, A. O., Lin, M. Y., and Moore, T.: Scientific assessment of background ozone over the US: Implications for air quality management, *Elementa: Science of the Anthropocene*, 6, 56, <https://doi.org/10.1525/elementa.309>, 2018.
- Janssens-Maenhout, G., Crippa, M., Guizzardi, D., Dentener, F., Muntean, M., Pouliot, G., Keating, T., Zhang, Q., Kurokawa, J., Wankmüller, R., Denier van der Gon, H., Kuenen, J. J. P., Klimont, Z., Frost, G., Darras, S., Koffi, B., and Li, M.: HTAP_v2.2: a mosaic of regional and global emission grid maps for 2008 and 2010 to study hemispheric transport of air pollution, *Atmos. Chem. Phys.*, 15, 11411–11432, <https://doi.org/10.5194/acp-15-11411-2015>, 2015.
- Judd, L. M., Al-Saadi, J. A., Szykman, J. J., Valin, L. C., Janz, S. J., Kowalewski, M. G., Eskes, H. J., Veefkind, J. P., Cede, A., Mueller, M., Gebetsberger, M., Swap, R., Pierce, R. B., Nowlan, C. R., Abad, G. G., Nehrir, A., and Williams, D.: Evaluating Sentinel-5P TROPOMI tropospheric NO₂ column densities with airborne and Pandora spectrometers near New York City and Long Island Sound, *Atmos. Meas. Tech.*, 13, 6113–6140, <https://doi.org/10.5194/amt-13-6113-2020>, 2020.
- Kang, D., Willison, J., Sarwar, G., Madden, M., Hogrefe, C., Mathur, R., Gantt, B., and Saiz-Lopez, A.: Improving the Characterization of Natural Emissions in CMAQ, *EM Magazine*, 30–36, 2021.
- Krotkov, N. A., Lamsal, L. N., Marchenko, S. V., and Swartz, W. H.: OMNO2 README Document, Data Product Version 4.0, NASA/Goddard Space Flight Center, <https://doi.org/10.5067/Aura/OMI/DATA2017>, 2019a.
- Krotkov, N. A., Lamsal, L. N., Marchenko, S. V., Bucsela, E. J., Swartz, W. H., Joiner, J., and the OMI/Aura Nitrogen Dioxide (NO₂) Total and Tropospheric Column 1-orbit L2 Swath 13 × 24 km V003, Goddard Earth Sciences Data and Information Services Center (GES DISC) [dataset], Greenbelt, MD, USA, <https://doi.org/10.5067/Aura/OMI/DATA2017>, 2019b.
- Kurokawa, J. and Ohara, T.: Long-term historical trends in air pollutant emissions in Asia: Regional Emission inventory in ASia (REAS) version 3, *Atmos. Chem. Phys.*, 20, 12761–12793, <https://doi.org/10.5194/acp-20-12761-2020>, 2020.
- Kurokawa, J., Yumimoto, K., Uno, I., and Ohara, T.: Adjoint inverse modeling of NO_x emissions over eastern China using satellite observations of NO₂ vertical column densities, *Atmos. Environ.*, 43, 1878–1887, <https://doi.org/10.1016/j.atmosenv.2008.12.030>, 2009.
- Lamsal, L. N., Martin, R. V., Padmanabhan, A., van Donkelaar, A., Zhang, Q., Sioris, C. E., Chance, K., Kurosu, T. P., and Newchurch, M. J.: Application of satellite observations for timely updates to global anthropogenic NO_x emission inventories, *Geophys. Res. Lett.*, 38, L05810, <https://doi.org/10.1029/2010gl046476>, 2011.
- Lamsal, L. N., Krotkov, N. A., Celarier, E. A., Swartz, W. H., Pickering, K. E., Bucsela, E. J., Gleason, J. F., Martin, R. V., Philip, S., Irie, H., Cede, A., Herman, J., Weinheimer, A., Szykman, J. J., and Knepp, T. N.: Evaluation of OMI operational standard NO₂ column retrievals using in situ and surface-based NO₂ observations, *Atmos. Chem. Phys.*, 14, 11587–11609, <https://doi.org/10.5194/acp-14-11587-2014>, 2014.
- Lamsal, L. N., Krotkov, N. A., Marchenko, S. V., Joiner, J., Oman, L., Vasilkov, A., Fisher, B., Qin, W., Yang, E.-S., Fasnacht, Z., Choi, S., Leonard, P., and Haffner, D.: OMI/Aura NO₂ Tropospheric, Stratospheric & Total Columns MINDS 1-Orbit L2 Swath 13 km x 24 km, Goddard Earth Sciences Data and Information Services Center (GES DISC) [dataset], <https://doi.org/10.5067/MEASURES/MINDS/DATA201>, 2020.

- Li, J. and Wang, Y.: Inferring the anthropogenic NO_x emission trend over the United States during 2003–2017 from satellite observations: was there a flattening of the emission trend after the Great Recession?, *Atmos. Chem. Phys.*, 19, 15339–15352, <https://doi.org/10.5194/acp-19-15339-2019>, 2019.
- Li, M., Klimont, Z., Zhang, Q., Martin, R. V., Zheng, B., Heyes, C., Cofala, J., Zhang, Y., and He, K.: Comparison and evaluation of anthropogenic emissions of SO₂ and NO_x over China, *Atmos. Chem. Phys.*, 18, 3433–3456, <https://doi.org/10.5194/acp-18-3433-2018>, 2018.
- Li, M., McDonald, B. C., McKeen, S. A., Eskes, H., Levelt, P., Francoeur, C., Harkins, C., He, J., Barth, M., Henze, D. K., Bela, M. M., Trainer, M., Gouw, J. A., and Frost, G. J.: Assessment of Updated Fuel-Based Emissions Inventories Over the Contiguous United States Using TROPOMI NO₂ Retrievals, *J. Geophys. Res.-Atmos.*, 126, e2021JD035484, <https://doi.org/10.1029/2021JD035484>, 2021.
- Luecken, D. J., Yarwood, G., and Hutzell, W. T.: Multipollutant modeling of ozone, reactive nitrogen and HAPs across the continental US with CMAQ-CB6, *Atmos. Environ.*, 201, 62–72, <https://doi.org/10.1016/j.atmosenv.2018.11.060>, 2019.
- Martin, R. V., Jacob, D. J., Chance, K., Kurosu, T. P., Palmer, P. I., and Evans, M. J.: Global inventory of nitrogen oxide emissions constrained by space-based observations of NO₂ columns, *J. Geophys. Res.-Atmos.*, 108, 4537, <https://doi.org/10.1029/2003jd003453>, 2003.
- Mathur, R., Xing, J., Gilliam, R., Sarwar, G., Hogrefe, C., Pleim, J., Pouliot, G., Roselle, S., Spero, T. L., Wong, D. C., and Young, J.: Extending the Community Multiscale Air Quality (CMAQ) modeling system to hemispheric scales: overview of process considerations and initial applications, *Atmos. Chem. Phys.*, 17, 12449–12474, <https://doi.org/10.5194/acp-17-12449-2017>, 2017.
- McDuffie, E. E., Smith, S. J., O'Rourke, P., Tibrewal, K., Venkataraman, C., Marais, E. A., Zheng, B., Crippa, M., Brauer, M., and Martin, R. V.: A global anthropogenic emission inventory of atmospheric pollutants from sector- and fuel-specific sources (1970–2017): an application of the Community Emissions Data System (CEDS), *Earth Syst. Sci. Data*, 12, 3413–3442, <https://doi.org/10.5194/essd-12-3413-2020>, 2020.
- Mijling, B. and van der A, R. J.: Using daily satellite observations to estimate emissions of short-lived air pollutants on a mesoscopic scale, *J. Geophys. Res.-Atmos.*, 117, D17302, <https://doi.org/10.1029/2012jd017817>, 2012.
- Miyazaki, K. and Eskes, H.: Constraints on surface NO_x emissions by assimilating satellite observations of multiple species, *Geophys. Res. Lett.*, 40, 4745–4750, <https://doi.org/10.1002/grl.50894>, 2013.
- Miyazaki, K., Eskes, H. J., and Sudo, K.: Global NO_x emission estimates derived from an assimilation of OMI tropospheric NO₂ columns, *Atmos. Chem. Phys.*, 12, 2263–2288, <https://doi.org/10.5194/acp-12-2263-2012>, 2012a.
- Miyazaki, K., Eskes, H. J., Sudo, K., Takigawa, M., van Weele, M., and Boersma, K. F.: Simultaneous assimilation of satellite NO₂, O₃, CO, and HNO₃ data for the analysis of tropospheric chemical composition and emissions, *Atmos. Chem. Phys.*, 12, 9545–9579, <https://doi.org/10.5194/acp-12-9545-2012>, 2012b.
- Miyazaki, K., Eskes, H., Sudo, K., Boersma, K. F., Bowman, K., and Kanaya, Y.: Decadal changes in global surface NO_x emissions from multi-constituent satellite data assimilation, *Atmos. Chem. Phys.*, 17, 807–837, <https://doi.org/10.5194/acp-17-807-2017>, 2017.
- Miyazaki, K., Bowman, K., Sekiya, T., Eskes, H., Boersma, F., Worden, H., Livesey, N., Payne, V. H., Sudo, K., Kanaya, Y., Takigawa, M., and Ogochi, K.: Chemical Reanalysis Products, Jet Propulsion Laboratory [dataset], <https://doi.org/10.25966/9qgv-fe81>, 2019.
- Miyazaki, K., Bowman, K., Sekiya, T., Eskes, H., Boersma, F., Worden, H., Livesey, N., Payne, V. H., Sudo, K., Kanaya, Y., Takigawa, M., and Ogochi, K.: Updated tropospheric chemistry reanalysis and emission estimates, TCR-2, for 2005–2018, *Earth Syst. Sci. Data*, 12, 2223–2259, <https://doi.org/10.5194/essd-12-2223-2020>, 2020.
- Müller, J.-F. and Stavrakou, T.: Inversion of CO and NO_x emissions using the adjoint of the IMAGES model, *Atmos. Chem. Phys.*, 5, 1157–1186, <https://doi.org/10.5194/acp-5-1157-2005>, 2005.
- Murray, C. J. L., Aravkin, A. Y., Zheng, P., Abbafati, C., Abbas, K. M., Abbasi-Kangevari, M., Abd-Allah, F., Abdelalim, A., Abdollahi, M., Abdollahpour, I., Abegaz, K. H., Abolhasani, H., Aboyans, V., Abreu, L. G., Abrigo, M. R. M., and Factors, G. R.: Global burden of 87 risk factors in 204 countries and territories, 1990–2019: a systematic analysis for the Global Burden of Disease Study 2019, *Lancet*, 396, 1223–1249, [https://doi.org/10.1016/S0140-6736\(20\)30752-2](https://doi.org/10.1016/S0140-6736(20)30752-2), 2020.
- Napelenok, S. L., Pinder, R. W., Gilliland, A. B., and Martin, R. V.: A method for evaluating spatially-resolved NO_x emissions using Kalman filter inversion, direct sensitivities, and space-based NO₂ observations, *Atmos. Chem. Phys.*, 8, 5603–5614, <https://doi.org/10.5194/acp-8-5603-2008>, 2008.
- Powers, J. G., Klemp, J. B., Skamarock, W. C., Davis, C. A., Dudhia, J., Gill, D. O., Coen, J. L., Gochis, D. J., Ahmadov, R., Peckham, S. E., Grell, G. A., Michalakes, J., Trahan, S., Benjamin, S. G., Alexander, C. R., Dimego, G. J., Wang, W., Schwartz, C. S., Romine, G. S., Liu, Z., Snyder, C., Chen, F., Barlage, M. J., Yu, W., and Duda, M. G.: The Weather Research and Forecasting Model: Overview, System Efforts, and Future Directions, *B. Am. Meteorol. Soc.*, 98, 1717–1737, <https://doi.org/10.1175/BAMS-D-15-00308.1>, 2017.
- Price, C., Penner, J., and Prather, M.: NO_x from lightning. 1. Global distribution based on lightning physics, *J. Geophys. Res.-Atmos.*, 102, 5929–5941, <https://doi.org/10.1029/96jd03504>, 1997.
- Qu, Z., Henze, D. K., Theys, N., Wang, J., and Wang, W.: Hybrid Mass Balance/4D-Var Joint Inversion of NO_x and SO₂ Emissions in East Asia, *J. Geophys. Res.-Atmos.*, 124, 8203–8224, <https://doi.org/10.1029/2018jd030240>, 2019.
- Qu, Z., Henze, D. K., Capps, S. L., Wang, Y., Xu, X. G., Wang, J., and Keller, M.: Monthly top-down NO_x emissions for China (2005–2012): A hybrid inversion method and trend analysis, *J. Geophys. Res.-Atmos.*, 122, 4600–4625, <https://doi.org/10.1002/2016jd025852>, 2017.
- Qu, Z., Jacob, D. J., Silvern, R. F., Shah, V., Campbell, P. C., Valin, L. C., and Murray, L. T.: US COVID-19 Shutdown Demonstrates Importance of Background NO₂ in Inferring NO_x Emissions From Satellite NO₂ Observations, *Geophys. Res. Lett.*, 48, e2021GL092783, <https://doi.org/10.1029/2021GL092783>, 2021.
- Salmon, O. E., Shepson, P. B., Ren, X., He, H., Hall, D. L., Dickerson, R. R., Stirr, B. H., Brown, S. S., Fibiger, D. L., McDuffie, E. E., Campos, T. L., Gurney, K. R.,

- and Thornton, J. A.: Top-Down Estimates of NO_x and CO Emissions From Washington, DC-Baltimore During the WINTER Campaign, *J. Geophys. Res.-Atmos.*, 123, 7705–7724, <https://doi.org/10.1029/2018jd028539>, 2018.
- Sandu, A. and Chai, T. F.: Chemical Data Assimilation-An Overview, *Atmosphere-Basel*, 2, 426–463, <https://doi.org/10.3390/atmos2030426>, 2011.
- Sekiya, T., Miyazaki, K., Ogochi, K., Sudo, K., Takigawa, M., Eskes, H., and Boersma, K. F.: Impacts of Horizontal Resolution on Global Data Assimilation of Satellite Measurements for Tropospheric Chemistry Analysis, *J. Adv. Model Earth Sy.*, 13, e2020MS002180, <https://doi.org/10.1029/2020MS002180>, 2021.
- Shao, H., Derber, J., Huang, X. Y., Hu, M., Newman, K., Stark, D., Lueken, M., Zhou, C. H., Nance, L., Kuo, Y. H., and Brown, B.: Bridging Research to Operations Transitions: Status and Plans of Community GSI, *B. Am. Meteorol. Soc.*, 97, 1427–1440, <https://doi.org/10.1175/BAMS-D-13-00245.1>, 2016.
- Silvern, R. F., Jacob, D. J., Mickley, L. J., Sulprizio, M. P., Travis, K. R., Marais, E. A., Cohen, R. C., Laughner, J. L., Choi, S., Joiner, J., and Lamsal, L. N.: Using satellite observations of tropospheric NO₂ columns to infer long-term trends in US NO_x emissions: the importance of accounting for the free tropospheric NO₂ background, *Atmos. Chem. Phys.*, 19, 8863–8878, <https://doi.org/10.5194/acp-19-8863-2019>, 2019.
- Simon, H., Reff, A., Wells, B., Xing, J., and Frank, N.: Ozone Trends Across the United States over a Period of Decreasing NO_x and VOC Emissions, *Environ. Sci. Technol.*, 49, 186–195, <https://doi.org/10.1021/es504514z>, 2015.
- Skamarock, W. C., Klemp, J. B., Dudhia, J., Gill, D. O., Barker, D. M., Duda, M. G., Huang, X. Y., Wang, W., and Powers, J. G.: A Description of the Advanced Research WRF Version 3, University Corporation for Atmospheric Research, NCAR Technical Notes, NCAR/TN-475+STR, 125 pp., <https://doi.org/10.5065/D68S4MVH>, 2008.
- Tong, D. Q., Lamsal, L., Pan, L., Ding, C., Kim, H., Lee, P., Chai, T. F., Pickering, K. E., and Stajner, I.: Long-term NO_x trends over large cities in the United States during the great recession: Comparison of satellite retrievals, ground observations, and emission inventories, *Atmos. Environ.*, 107, 70–84, <https://doi.org/10.1016/j.atmosenv.2015.01.035>, 2015.
- Tong, D. Q., Pan, L., Chen, W. W., Lamsal, L., Lee, P., Tang, Y. H., Kim, H., Kondragunta, S., and Stajner, I.: Impact of the 2008 Global Recession on air quality over the United States: Implications for surface ozone levels from changes in NO_x emissions, *Geophys. Res. Lett.*, 43, 9280–9288, <https://doi.org/10.1002/2016gl069885>, 2016.
- Toro, C., Foley, K., Simon, H., Henderson, B., Baker, K. R., Eyth, A., Timin, B., Appel, W., Lueken, D., Beardsley, M., Sonntag, D., Possiel, N., and Roberts, S.: Evaluation of 15 years of modeled atmospheric oxidized nitrogen compounds across the contiguous United States, *Elementa: Science of the Anthropocene*, 9, 00158, <https://doi.org/10.1525/elementa.2020.00158>, 2021.
- Turner, A. J., Henze, D. K., Martin, R. V., and Hakami, A.: The spatial extent of source influences on modeled column concentrations of short-lived species, *Geophys. Res. Lett.*, 39, L12806, <https://doi.org/10.1029/2012gl015832>, 2012.
- U.S. EPA (U.S. Environmental Protection Agency): Air Pollutant Emissions Trends Data, <https://www.epa.gov/air-emissions-inventories/air-pollutant-emissions-trends-data>, last access: 9 December 2022a.
- U.S. EPA (U.S. Environmental Protection Agency): Air Quality System (AQS), <https://www.epa.gov/aqs>, last access: 9 December 2022b (data available at: https://aqs.epa.gov/aqswb/airdata/download_files.html, last access: 9 December 2022).
- US EPA Office of Research and Development: CMAQ, Version 5.3.2, Zenodo [code], <https://doi.org/10.5281/zenodo.4081737>, 2020 (code available at: <https://github.com/usepa/cmaq.git>, last access: 9 December 2022).
- Valin, L. C., Russell, A. R., Hudman, R. C., and Cohen, R. C.: Effects of model resolution on the interpretation of satellite NO₂ observations, *Atmos. Chem. Phys.*, 11, 11647–11655, <https://doi.org/10.5194/acp-11-11647-2011>, 2011.
- van Geffen, J., Eskes, H. J., Boersma, K. F., Maasakkers, J. D., and Veefkind, J. P.: TROPOMI ATBD of the total and tropospheric NO₂ data products, Royal Netherlands Meteorological Institute, S5P-KNMI-L2-0005-RP, 2019.
- van Geffen, J., Boersma, K. F., Eskes, H., Sneep, M., ter Linden, M., Zara, M., and Veefkind, J. P.: SSP TROPOMI NO₂ slant column retrieval: method, stability, uncertainties and comparisons with OMI, *Atmos. Meas. Tech.*, 13, 1315–1335, <https://doi.org/10.5194/amt-13-1315-2020>, 2020.
- van Geffen, J., Eskes, H., Compennolle, S., Pinardi, G., Verhoelst, T., Lambert, J.-C., Sneep, M., ter Linden, M., Ludewig, A., Boersma, K. F., and Veefkind, J. P.: Sentinel-5P TROPOMI NO₂ retrieval: impact of version v2.2 improvements and comparisons with OMI and ground-based data, *Atmos. Meas. Tech.*, 15, 2037–2060, <https://doi.org/10.5194/amt-15-2037-2022>, 2022.
- Veefkind, J. P., Aben, I., McMullan, K., Forster, H., de Vries, J., Otter, G., Claas, J., Eskes, H. J., de Haan, J. F., Kleipool, Q., van Weele, M., Hasekamp, O., Hoogeveen, R., Landgraf, J., Snel, R., Tol, P., Ingmann, P., Voors, R., Kruizinga, B., Vink, R., Visser, H., and Levelt, P. F.: TROPOMI on the ESA Sentinel-5 Precursor: A GMES mission for global observations of the atmospheric composition for climate, air quality and ozone layer applications, *Remote Sens. Environ.*, 120, 70–83, <https://doi.org/10.1016/j.rse.2011.09.027>, 2012.
- Verhoelst, T., Compennolle, S., Pinardi, G., Lambert, J.-C., Eskes, H. J., Eichmann, K.-U., Fjæraa, A. M., Granville, J., Niemeijer, S., Cede, A., Tiefengraber, M., Hendrick, F., Pazmiño, A., Bais, A., Bazureau, A., Boersma, K. F., Bognar, K., Dehn, A., Donner, S., Elokhov, A., Gebetsberger, M., Goutail, F., Grutter de la Mora, M., Gruzdev, A., Gratsea, M., Hansen, G. H., Irie, H., Jepsen, N., Kanaya, Y., Karagkiozidis, D., Kivi, R., Kreher, K., Levelt, P. F., Liu, C., Müller, M., Navarro Comas, M., Piters, A. J. M., Pommereau, J.-P., Portafaix, T., Prados-Roman, C., Puente-dura, O., Querel, R., Remmers, J., Richter, A., Rimmer, J., Rivera Cárdenas, C., Saavedra de Miguel, L., Sinyakov, V. P., Stremme, W., Strong, K., Van Roozendaal, M., Veefkind, J. P., Wagner, T., Wittrock, F., Yela González, M., and Zehner, C.: Ground-based validation of the Copernicus Sentinel-5P TROPOMI NO₂ measurements with the NDACC ZSL-DOAS, MAX-DOAS and Pandora global networks, *Atmos. Meas. Tech.*, 14, 481–510, <https://doi.org/10.5194/amt-14-481-2021>, 2021.
- Verstraeten, W. W., Neu, J. L., Williams, J. E., Bowman, K. W., Worden, J. R., and Boersma, K. F.: Rapid increases in tropo-

- spheric ozone production and export from China, *Nat. Geosci.*, 8, 690–695, <https://doi.org/10.1038/ngeo2493>, 2015.
- Visser, A. J., Boersma, K. F., Ganzeveld, L. N., and Krol, M. C.: European NO_x emissions in WRF-Chem derived from OMI: impacts on summertime surface ozone, *Atmos. Chem. Phys.*, 19, 11821–11841, <https://doi.org/10.5194/acp-19-11821-2019>, 2019.
- Wang, C. J., Wang, T., Wang, P. C., and Rakitin, V.: Comparison and Validation of TROPOMI and OMI NO₂ Observations over China, *Atmosphere-Basel*, 11, 636, <https://doi.org/10.3390/atmos11060636>, 2020.
- Wang, Y., Wang, J., Xu, X., Henze, D. K., Qu, Z., and Yang, K.: Inverse modeling of SO₂ and NO_x emissions over China using multisensor satellite data – Part 1: Formulation and sensitivity analysis, *Atmos. Chem. Phys.*, 20, 6631–6650, <https://doi.org/10.5194/acp-20-6631-2020>, 2020.
- Wiedinmyer, C., Akagi, S. K., Yokelson, R. J., Emmons, L. K., Al-Saadi, J. A., Orlando, J. J., and Soja, A. J.: The Fire INventory from NCAR (FINN): a high resolution global model to estimate the emissions from open burning, *Geosci. Model Dev.*, 4, 625–641, <https://doi.org/10.5194/gmd-4-625-2011>, 2011.
- WOUDC (World Ozone and Ultraviolet Data Center): OzoneSonde data, WOUDC [dataset], <https://doi.org/10.14287/10000008>, 2019.
- Xing, J., Mathur, R., Pleim, J., Hogrefe, C., Gan, C.-M., Wong, D. C., and Wei, C.: Can a coupled meteorology–chemistry model reproduce the historical trend in aerosol direct radiative effects over the Northern Hemisphere?, *Atmos. Chem. Phys.*, 15, 9997–10018, <https://doi.org/10.5194/acp-15-9997-2015>, 2015.
- Xu, L., Pye, H. O. T., He, J., Chen, Y., Murphy, B. N., and Ng, N. L.: Experimental and model estimates of the contributions from biogenic monoterpenes and sesquiterpenes to secondary organic aerosol in the southeastern United States, *Atmos. Chem. Phys.*, 18, 12613–12637, <https://doi.org/10.5194/acp-18-12613-2018>, 2018.
- Zhang, L., Jacob, D. J., Boersma, K. F., Jaffe, D. A., Olson, J. R., Bowman, K. W., Worden, J. R., Thompson, A. M., Avery, M. A., Cohen, R. C., Dibb, J. E., Flock, F. M., Fuelberg, H. E., Huey, L. G., McMillan, W. W., Singh, H. B., and Weinheimer, A. J.: Transpacific transport of ozone pollution and the effect of recent Asian emission increases on air quality in North America: an integrated analysis using satellite, aircraft, ozonesonde, and surface observations, *Atmos. Chem. Phys.*, 8, 6117–6136, <https://doi.org/10.5194/acp-8-6117-2008>, 2008.
- Zhang, X., Jones, D. B. A., Keller, M., Walker, T. W., Jiang, Z., Henze, D. K., Worden, H. M., Bourassa, A. E., Dengenstein, D. A., and Rochon, Y. J.: Quantifying Emissions of CO and NO_x Using Observations From MOPITT, OMI, TES, and OSIRIS, *J. Geophys. Res.-Atmos.*, 124, 1170–1193, <https://doi.org/10.1029/2018jd028670>, 2019.
- Zhang, Y. Q., Cooper, O. R., Gaudel, A., Thompson, A. M., Nedelec, P., Ogino, S. Y., and West, J. J.: Tropospheric ozone change from 1980 to 2010 dominated by equatorward redistribution of emissions, *Nat. Geosci.*, 9, 875–879, <https://doi.org/10.1038/Ngeo2827>, 2016.
- Zhao, B., Zheng, H. T., Wang, S. X., Smith, K. R., Lu, X., Aunan, K., Gu, Y., Wang, Y., Ding, D., Xing, J., Fu, X., Yang, X. D., Liou, K. N., and Hao, J. M.: Change in household fuels dominates the decrease in PM_{2.5} exposure and premature mortality in China in 2005–2015, *P. Natl. Acad. Sci. USA*, 115, 12401–12406, <https://doi.org/10.1073/pnas.1812955115>, 2018.
- Zhu, Y. Z., Hu, Q. H., Gao, M., Zhao, C., Zhang, C. X., Liu, T., Tian, Y., Yan, L., Su, W. J., Hong, X. H., and Liu, C.: Quantifying Contributions of Local Emissions and Regional Transport to NO_x in Beijing Using TROPOMI Constrained WRF-Chem Simulation, *Remote Sens.-Basel*, 13, 1798, <https://doi.org/10.3390/rs13091798>, 2021.